Agricultural Water Management 321 (2025) 109941

Contents lists available at ScienceDirect

Agricultural Water Management

journal homepage: www.elsevier.com/locate/agwat

Spatiotemporal dynamics of actual evapotranspiration and its attribution analysis in dryland regions of Northwest China

Kaixuan Liu [a,b,c], Haibo Wang [a,b,*], Jingfeng Xiao [d], Kun Zhang [e], Gaofeng Zhu [f], Xufeng Wang [a], Yi'na Hu [g], Yi Song [h], Junlei Tan [a], Liying Geng [a]

[a] *State Key Laboratory of Cryospheric Science and Frozen Soil Engineering, Key Laboratory of Remote Sensing of Gansu Province, Heihe Remote Sensing Experimental Research Station, Northwest Institute of Eco-Environment and Resources, Chinese Academy of Sciences, Lanzhou 730000, China*

[b] *State Key Laboratory of Ecological Safety and Sustainable Development in Arid Lands, Northwest Institute of Eco-Environment and Resources, Chinese Academy of Sciences, Lanzhou 730000, China*

[c] *University of Chinese Academy of Sciences, Beijing 100049, China*

[d] *Earth Systems Research Center, Institute for the Study of Earth, Oceans, and Space, University of New Hampshire, Durham, NH 03824, USA*

[e] *School of Geospatial Engineering and Science, Sun Yat-Sen University, Zhuhai, China*

[f] *Key Laboratory of Western China's Environmental Systems (Ministry of Education), College of Earth and Environmental Sciences, Lanzhou University, Lanzhou 730000, China*

[g] *School of Environmental and Geographical Sciences, Shanghai Normal University, Shanghai 200234, China*

[h] *Institute of Earth Environment, Chinese Academy of Sciences, Xi'an 710061, China*

A R T I C L E I N F O

Handling Editor - X Zhang

Keywords:
ET estimation
PT-JPL model
Parameter optimization
Eddy covariance
Arid and semi-arid regions
Google Earth Engine

A B S T R A C T

Evapotranspiration (ET) is a fundamental process linking the energy, water, and carbon cycles in terrestrial ecosystems. In dryland regions like Northwest China, where water availability strongly constrains ecosystem functioning, understanding the spatiotemporal dynamics of actual evapotranspiration (ET_a) and its controlling mechanisms is critical for ecohydrological assessments under climate change. However, these regions face persistent challenges due to sparse vegetation, heterogeneous soils, and limited observations, which impede accurate regional-scale ET_a quantification and attribution analysis. This study investigates the spatiotemporal patterns and controlling factors of ET_a in Northwest China from 2001 to 2024 using the Priestley-Taylor Jet Propulsion Laboratory (PT-JPL) model optimized with remote sensing and flux observations. The model was optimized using 16 flux towers, achieving an R^2 of 0.74 and enabling reliable regional ET_a estimation under data-scarce conditions. The optimized model produced multi-year average ET_a of 292.2 mm and an increasing trend of 0.43 mm yr^{-1}. ET_a exhibited a clear spatial gradient, higher in the east, lower in the west, corresponding to vegetation and water availability. Importantly, standardized ridge regression revealed that environmental factors explained 83.4 % of ET_a variability, with relative humidity alone contributing the largest share (33.6 %). Vegetation dynamics accounted for 16.6 %, primarily associated with farmland expansion and afforestation. This findings offer a robust framework for disentangling ET_a drivers in data-scarce drylands and underscore the dominant role of both atmospheric humidity and land cover change in shaping regional evapotranspiration patterns. This study delivers valuable insights for sustainable water and land resource management under climate change.

1. Introduction

Evapotranspiration (ET) plays a fundamental role in linking terrestrial energy, water, and carbon cycles (Fisher et al., 2008; Li et al., 2023). Globally, more than 60 % of precipitation returns to the atmosphere through ET (Jasechko et al., 2013), and rising ET rates driven by climate change are exacerbating hydrological extremes (Oki and Kanae, 2006). In dryland regions, ET is influenced by complex interactions among climate, vegetation, and water availability, particularly soil moisture and groundwater (Wang et al., 2023, 2021). Land use

* Corresponding author at: State Key Laboratory of Cryospheric Science and Frozen Soil Engineering, Key Laboratory of Remote Sensing of Gansu Province, Heihe Remote Sensing Experimental Research Station, Northwest Institute of Eco-Environment and Resources, Chinese Academy of Sciences, Lanzhou 730000, China.

E-mail address: whb@lzb.ac.cn (H. Wang).

https://doi.org/10.1016/j.agwat.2025.109941

Received 27 February 2025; Received in revised form 21 October 2025; Accepted 26 October 2025

Available online 30 October 2025

and land cover changes caused by human activities further reshape ET patterns by altering vegetation structure and surface properties (Wang et al., 2014; Li et al., 2016). These shifts have important implications for ecosystem functions, hydrological processes, and water resource sustainability. Given that ET serves as a key exchange flux between terrestrial ecosystems and the atmosphere (Zhao et al., 2020), accurately monitoring its dynamics and identifying dominant driving factors is essential for understanding ecohydrological feedbacks under climate change. ET primarily comprises soil evaporation and vegetation transpiration, which respond differently to environmental drivers. While soil evaporation is regulated by surface and atmospheric conditions, vegetation transpiration is mainly related to the growth status of vegetation, soil water availability, and environmental conditions (Hu et al., 2024; Wang et al., 2021). Consequently, ET spatiotemporal variability is jointly driven by air temperature, humidity, precipitation, radiation, vegetation activity, and water availability (Hu et al., 2024; Li et al., 2022; Ma and Zhang, 2022). Dryland regions—accounting for over 40 % of the global land surface—are especially vulnerable to climate extremes and human disturbance (Wang et al., 2023, 2019b). Northwest China (NWC) is a representative dryland region facing persistent water scarcity, high potential ET, and fragile ecological conditions (Wang et al., 2021, 2019a). Although previous studies have examined ET patterns and their drivers across multiple spatial scales (Liu et al., 2021; Ma and Zhang, 2022; Niu et al., 2019; Yang et al., 2022; Zhao et al., 2023), most assessments rely on coarse-resolution data or general regression models. As a result, the relative contributions of climatic, biological, and subsurface hydrological factors to ET variability in data-scarce drylands remain insufficiently quantified. This knowledge gap limits the ability to support water resource planning under climate change.

Although numerous remote sensing products are available at various spatiotemporal resolutions, significant uncertainties persist between different datasets, with potential discrepancies reaching up to 30 % (Zou et al., 2017). As research on ET continues to grow, a wide range of remote sensing-based models have been developed to address these challenges (Bastiaanssen et al., 1998; Mu et al., 2011; Zhang et al., 2019). These include energy balance-based models such as METRIC (Allen et al., 2007), SEBAL (Bastiaanssen et al., 1998) and TSEB (Kustas and Norman, 1999), as well as physical or semi-empirical models like MOD16 (Mu et al., 2011) and PML (Zhang et al., 2019). Energy balance models rely on high-resolution thermal data and are well-suited for field- to watershed-scale applications; however, they may face limitations in large-scale, long-term monitoring due to data availability and computational complexity. In contrast, models such as MOD16 and PML provide physically based yet operationally efficient alternatives that are particularly useful for regional- to global-scale ET estimation. Nevertheless, these products often lack sufficient validation in arid ecosystems due to sparse flux tower coverage, leading to considerable uncertainties when applied in drylands such as NWC. Among various models, the Priestley-Taylor Jet Propulsion Laboratory (PT-JPL) model (Fisher et al., 2008) stands out by addressing the limitations of the Penman-Monteith (PM) model, particularly the uncertainty related to canopy and aerodynamic resistance. Its minimal parameterization requirements and compatibility with satellite-derived inputs make it especially suitable for data-scarce, heterogeneous dryland regions (Li et al., 2022). Furthermore, the availability of cloud-based platforms such as Google Earth Engine (GEE) greatly facilitates the implementation of large-scale ET modeling and analysis.

Although ET models including PT-JPL have been widely used, the simulated ET may exhibit significant instability due to uncertainties in model structure, input data, and parameters (Wang et al., 2019a). In-situ ET flux observations, particularly from eddy covariance (EC) towers, provide a valuable basis for model calibration and have been widely utilized to optimize parameters (Niu et al., 2020; Zhang et al., 2017). Among optimization techniques, the Markov chain Monte Carlo (MCMC) approach is commonly employed to quantify model uncertainty and optimize parameters (Zhu et al., 2014; Wang et al., 2019a), though it often suffers from slow convergence (Haario et al., 2006). To address these issues, we adopted the Differential Evolution Markov Chain (DE-MC) algorithm, which integrates global optimization capabilities of differential evolution and is better suited for high-dimensional parameter calibration (Braak, 2006). This enabled land cover-specific parameter optimization of the PT-JPL model across six typical ecosystem types in NWC.

While ET drivers have been extensively studied at local and global scales, few studies have conducted regionally calibrated and observation-constrained assessments that integrate vegetation, climate, and groundwater influences in arid zones. Traditional multiple regression methods are often limited by multicollinearity (Li et al., 2022; Yang et al., 2022), whereas ridge regression has been shown to effectively isolate the relative effects of vegetation and climatic variables on ETa (Katul et al., 2012; Zhao et al., 2023). This is especially important in heterogeneous dryland environments, where the interplay between vegetation dynamics, subsurface water availability, and meteorological forcing remains poorly understood.

In this study, we optimized the PT-JPL model with remote sensing and EC data and then used the optimized model to quantify ET_a dynamics in NWC from 2001 to 2024. Specifically, we aimed: (1) to investigate the spatiotemporal patterns of ET_a based on land cover-specific model calibration; (2) to assess the relative contributions of vegetation dynamics, climatic variables, and water availability using partial correlation and ridge regression; and (3) to explore how land use change modulates ET_a patterns. This framework provides an improved basis for understanding water cycle dynamics and informing water resources management strategies in dryland regions.

2. Materials and methods

2.1. Study area

Northwestern China, located in the interior of Eurasia, encompasses the provinces or autonomous regions of Ningxia, Xinjiang, Gansu, Qinghai, and Shaanxi, along with the western portion of Inner Mongolia (i.e., Alxa League), covering an area of approximately 3.53 million km^2. The region's terrain is complex, dominated by a mix of plateaus, mountains, and basins (Fig. 1). Major mountain ranges, including the Qinling, Qilian, Tianshan and Kunlun Mountains, among others, not only provide the topographical backbone of the region but also crucial water sources for oasis agriculture (Chen et al., 2015). Key geographical units, such as the Qinghai-Tibet Plateau (QTP), Tarim Basin, Junggar Basin, Taklamakan Desert, Hexi Corridor, Loess Plateau, and Qaidam Basin, are characterized by towering mountains and expansive basins (Wang et al., 2020).

The region experiences a mix of temperate continental and alpine climates, with some areas influenced by a temperate monsoon climate in the southeast. This diverse climatic pattern (Yang et al., 2022), along with high temperature variability (average annual temperature of approximately 4.5°C, with extremes ranging from −30°C and 40°C), is reflected in its fragile and sensitive ecosystems (Katul et al., 2012; Shi et al., 2007). Precipitation is extremely low, with one-third of the region receiving less than 50 mm annually. The region's precipitation gradient varies from 200 mm to 800 mm depending on the elevation and proximity to mountains, with higher amounts concentrated in the southeastern regions (Chi et al., 2023; Liang et al., 2023). The diverse climatic conditions and the fragile ecosystem in this region play a crucial role in shaping the region's water balance and ET dynamics.

2.2. Eddy covariance data processing and quality control

The eddy covariance (EC) technique is a well-established method for measuring ET and validating ET estimation models (Lin et al., 2024; Wang et al., 2021). Through continuously measuring high-frequency water vapor exchange at the ecosystem scale, EC observations can

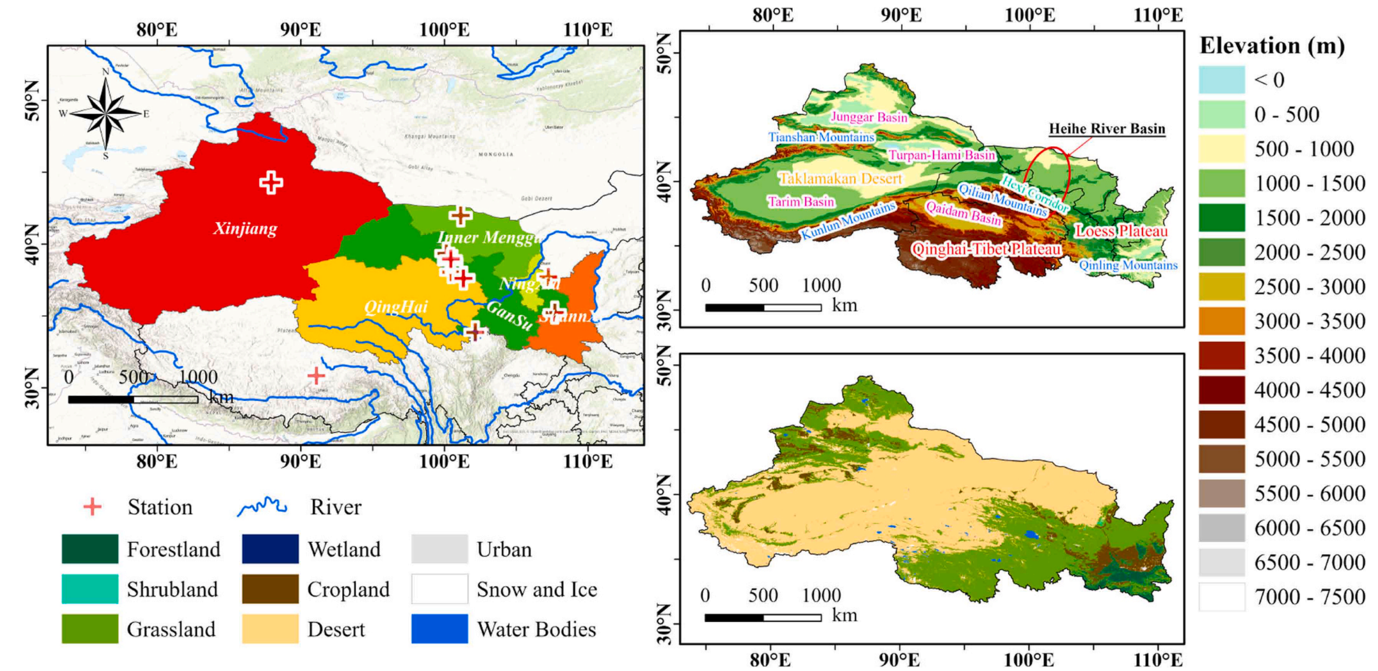

Fig. 1. Study area of Northwest China, and the eddy covariance (EC) flux sites, along with the elevation and land cover type distributions. Additional information on the EC sites is presented in Table 1.

directly capture the temporal dynamics of ET. EC flux observations have been extensively utilized to investigate the variations of ET at regional scales widely (Wang et al., 2021). In this study, we selected a total of 16 flux tower sites in NWC and neighboring areas to validate the model. These sites represent diverse dryland ecosystem types across NWC. The EC flux tower data were collected from the ChinaFLUX (Yu et al., 2006, 2016), the HiWATER datasets in the Heihe River Basin (HRB) (Liu et al., 2023; 2018), the dataset of Coordinated Observations and Integrated Research over Arid and Semi-arid China (COIRAS) (Wang et al., 2013a). Detailed metadata and references for each site are listed in Table 1.

The flux data were measured by an open-path EC system (i.e., CSAT-3, Campbell Sci. Ins. Inc., USA; and Li-7500A, Li-Cor Inc., USA), which were underwent standardized and rigorous quality control and correction procedures. These included spike detection, sonic temperature correction, coordinate rotation, frequency response correction, and WPL correction (Webb et al., 1980; Yu et al., 2006; Liu et al., 2018; Wang et al., 2019b; Wang et al., 2013b). The raw 10 Hz EC data were processed into half-hourly fluxes a with data quality flags according to the stationary test (Allen et al., 2011; Foken et al., 2004; Liu et al., 2018). Based on site-specific publications and our calculations for the study period, average EBR values across all sites ranged from 0.71 to 0.95 (overall mean 0.84; Table S1), exceeding the commonly accepted threshold ($\approx$0.7). Thus, the EC datasets are considered robust for model evaluation. Further details on the data processing and site-specific fetch characteristics for these sites can be found in the original site documentation referenced in Table 1.

2.3. Other data sources and processing

In this study, we utilize various remote sensing derived data and meteorological datasets to run the model. At the site scale, meteorological data such as net radiation, relative humidity, and air temperature were derived from tower-based observational data. The processing procedures of the meteorological data for each site was described in the corresponding references in the Table 1.

The NDVI and Enhanced Vegetation Index (EVI) data were extracted from the MOD13A1 V6.1 dataset of MODIS (https://modis.gsfc.nasa.gov/), with a spatial resolution of 500 meters and temporal resolution of 16 days. The land cover type data for Northwestern China from 2001 to 2024 were obtained from the MODIS MCD12Q1 V6.1 product (https://modis.gsfc.nasa.gov/), which is based on the Annual International Geosphere-Biosphere Programme (IGBP) classification with a spatial resolution of 500 m. The land cover types were then reclassified

Table 1
The location, duration, vegetation type, and reference for the 16 EC sites used in this study.

Name	Lon (°N)	Lat (°E)	Time span	Type	Reference
A'rou	100.46	38.05	2013–2018	Grassland	(Liu et al., 2023, 2018)
Haibei grassland	101.31	37.61	2015–2020	Grassland	(Zhang et al., 2023b)
Maqu	102.15	33.86	2014–2019	Grassland	(Meng et al., 2023)
Changwu	107.68	35.23	2008–2009	Cropland	(Wang et al., 2013b)
Daman	100.37	38.86	2013–2017	Cropland	(Liu et al., 2023, 2018)
Linze	100.13	39.35	2012–2015	Cropland	(Ji et al., 2023)
Yingke	100.42	38.85	2008–2009	Cropland	(Liu et al., 2023, 2018)
Dangxiong	91.08	30.85	2004–2010	Forestland	(Chai et al., 2021)
Hunhelin	101.13	41.99	2015–2020	Forestland	(Liu et al., 2023, 2018)
Haibei shrubland	101.33	37.67	2011–2020	Shrubland	(Zhang et al., 2023a)
Yanchi	107.23	37.71	2012–2016	Shrubland	(Han et al., 2023)
Huazhaizi	100.32	38.77	2013–2017	Desert	(Liu et al., 2023, 2018)
Shenshawo	100.49	38.79	2012–2014	Desert	(Liu et al., 2023, 2018)
Fukang	87.93	44.28	2009	Desert	(Liu et al., 2012)
Haibei wetland	101.32	37.60	2004–2009	Wetland	(Zhang et al., 2021)
Zhangye wetland	100.45	38.98	2013–2017	Wetland	(Liu et al., 2023, 2018)

into broad categories including forestland, shrubland, grassland, wetland, cropland, desert and others for the ET simulation process.

At the regional scale, meteorological forcing was obtained from the NASA Global Land Data Assimilation System V2.1 (GLDAS-2.1) reanalysis datasets at 3-hourly resolution. We synthesized relevant meteorological variables such as precipitation, relative humidity, net solar radiation, soil moisture, and air temperature to daily values and then complied into 8-day composites for the model runs. All variables were resampled to match with spatial resolution of the MODIS products (500 m) using bilinear interpolation. Data processing and model execution were performed on the GEE platform. GLDAS-2.1 driver data showed strong agreement with flux tower meteorological observations in this study (Supplementary Fig. S1), supporting its reliability as input for regional-scale modeling in NWC. For groundwater depth (GWD) data, we used the GWD data derived from the long-term observational data of China Geological Environment Monitoring Groundwater Level Yearbook (2005–2022) developed by Wang et al. (2025). We extracted annual GWD composites for NWC from 2005 to 2022 and resampled them to 500 m spatial resolution using bilinear interpolation.

2.4. The ET model and parameter optimization

The Priestley-Taylor model was first proposed in 1972 for the estimation of potential evapotranspiration, and its theory and accuracy have been validated (Priestley and Taylor, 1972). The general form is as follows:

$$LE = \alpha\frac{\Delta}{\Delta+\gamma}(R_n - G) \tag{1}$$

Fisher et al. (2008) developed the Priestly-Taylor Jet Propulsion Laboratory (PT-JPL) model, which integrates remotely sensed data and directly calculates the actual ET (ET_a). The model separates the final evapotranspiration into three parts: transpiration from plant canopy (LE_c), soil evaporation (LE_s), as well as interception evaporation (LE_i). The specific equations of the PT-JPL model are provided in Table 2.

where f_{wet} is the relative surface moisture limitation factor; f_{sm} is the soil moisture limitation factor; f_g, f_t and f_m are the limitation factor of green canopy, temperature, and moisture, respectively. R_n refers to the net radiation; R_{nc} and R_{ns} represent the portion of net radiation absorbed by the vegetation canopy and the soil surface, respectively; G corresponds to the soil heat flux; α denotes the Priestley-Taylor coefficient (set to 1.26); γ stands the psychrometric constant; and Δ denotes the gradient of the saturation vapor pressure curve.

In Bayesian theory, the posterior probability density function (PDF) for the model parameters (θ), conditioned on the observations (O) (i.e., $p(\theta|O)$) is determined using prior knowledge about the parameters and the information obtained from model validations. This relationship is formulated as follows (Wang et al., 2019a):

$$p(\theta|O) = \frac{p(\theta)p(O|\theta)}{p(O)} \tag{2}$$

where $p(\theta)$ and $p(O)$ denote the prior probability distribution of parameters and posterior probability distribution of observations, respectively, while $p(O|\theta)$ represents the conditional probability density of ET observations based on prior information. For a dataset containing N observations, $p(\theta)$ can be defined as (Zhu et al., 2014):

$$p(\theta) = \prod_{i=1}^{N}\frac{1}{\sqrt{2\pi}\sigma}e^{-\frac{(Obs_i - Sim_i)^2}{2\sigma^2}} \tag{3}$$

Here, Obs_i denotes the i-th observation in a set of N data points; Sim_i represents the i-th of N simulation data (Braswell et al., 2005). The term σ is given as:

$$\sigma = \sqrt{\frac{1}{N}\sum_{i=1}^{N}(Obs_i - Sim_i)^2} \tag{4}$$

Table 2
Key Parameters and Equations of the PT-JPL Model for ET Estimation.

Parameter	Description	Equation	Reference
LE_a	Latent heat flux	$LE_c + LE_s + LE_i$	(Fisher et al., 2008)
LE_c	Transpiration from plant canopy	$(1 - f_{wet})f_g f_t f_m \alpha\frac{\Delta}{\Delta+\gamma}R_{nc}$	(Fisher et al., 2008; Priestley and Taylor, 1972)
LE_s	Soil evaporation	$(f_{wet} + f_{sm}(1 - f_{wet}))\alpha\frac{\Delta}{\Delta+\gamma}(R_{ns} - G)$	(Fisher et al., 2008; Priestley and Taylor, 1972)
LE_i	Interception evaporation	$f_{wet}\alpha\frac{\Delta}{\Delta+\gamma}R_{nc}$	(Fisher et al., 2008)
f_{wet}	Relative surface moisture limitation factor	RH^4	(Fisher et al., 2008)
f_{sm}	Soil moisture limitation factor	$RH^{VPD/\beta}$	(Fisher et al., 2008)
f_g	Limitation factor of green canopy	f_{APAR}/f_{IPAR}	(Fisher et al., 2008)
f_t	Limitation factor of temperature	$e^{-((T_a - T_{opt})/T_{opt})^2}$	(Niu et al., 2019)
f_m	Limitation factor of moisture	$f_{APAR}/f_{APAR\max}$	(Fisher et al., 2008)
R_{nc}	Net radiation to the vegetation	$R_n - R_{ns}$	(Beer, 1852; Denmead and Millar, 1976)
R_{ns}	Net radiation to the soil	$R_n\exp(-k_{Rn}LAI)$	(Beer, 1852; Denmead and Millar, 1976)
f_{APAR}	Fraction of photosynthesis active radiation	$m_1EVI + b_1$	(Fisher et al., 2008; Gao, 2000; Huete et al., 2002)
f_{IPAR}	Fraction of PAR absorbed by the canopy	$m_2NDVI + b_2$	(Fisher et al., 2008; Gao, 2000; Huete et al., 2002)

By integrating the PT-JPL model with the EC flux tower based ET observations, we applied the DE-MC algorithm in optimizing the model's sensitive parameters: m1, b1 and β in the model. The DE-MC algorithm, based on swarm intelligence, incorporates features of the differential evolution algorithm and the MCMC method (Braak, 2006). In this approach, N chains are run simultaneously, and proposals are generated using two randomly selected chains. This method helps to reduce the prior uncertainty of sensitive parameters and enhances the model's accuracy. To improve regional parameter generalization, we classified the 16 flux tower sites into six dominant vegetation types based on MODIS land cover data (MCD12Q1 V6.1), and optimized PT-JPL parameters separately for each type. The resulting parameter sets were then applied spatially according to land cover distribution. Model optimization was evaluated using the Nash-Sutcliffe Efficiency

(NSE), a robust, dimensionless indicator commonly used in ecohydrological modeling.

2.5. Statistical analysis

2.5.1. ET trend analysis

To evaluate the annual variation trends of the optimized ET simulations in the Northwest Territories from 2001 to 2024, a linear regression model was applied based on the least squares approach. The ET trend, i.e., the slope of the linear model (θ_{slope}) was calculated using the following formula (Luo et al., 2018; Ren et al., 2022):

$$\theta_{slope} = \frac{n\sum_{i=1}^{n} iET_i - \sum_{i=1}^{n} i\sum_{i=1}^{n} ET_i}{n\sum_{i=1}^{n} i^2 - \left(\sum_{i=1}^{n} i\right)^2} \tag{5}$$

where n is the number of years in the ET time series; and ET_i refers to the annual cumulated ET for the i-th year. A positive value of θ_{slope} refers to an upward trend in ET over the study period. Conversely, a negative θ suggests a decrease in ET during the study period. Additionally, θ = zero implies no change in ET. The T-test was utilized to evaluate the significance of the ET trend over time.

2.5.2. Partial correlation analysis

We employed partial correlation analysis to examine the relationship between ET and various influencing factors. This technique allows us to assess the impact of each variable while keeping the others constant. We analyzed how ET relates to each specific variable, considering the other five variables as controls. The detailed formula for $R_{xy,z(i)}$, which denotes the partial correlation coefficient between variables x and y while accounting for the effect of z(i), is provided below (Gu et al., 2018; Liu et al., 2024; Marrelec et al., 2006):

$$R_{xy,\ z(i)} = \frac{R_{xy} - R_{xz(i)} \bullet R_{yz(i)}}{\sqrt{\left(1 - {R_{xz(i)}}^2\right) \bullet \left(1 - {R_{yz(i)}}^2\right)}} \tag{6}$$

In this equation, R_{xy}, $R_{xz(i)}$, and $R_{yz(i)}$ indicate the correlation coefficients between x, y, and $z(i)$, respectively.

2.5.3. Relative contributions of the controlling factors

In dryland regions, ET is governed not only by atmospheric demand but also by the availability of water. Therefore, both energy-related and moisture-related variables were included to better represent the ecohydrological constraints on ET dynamics. We utilized standardized ridge regression to investigate the contributions of various factors to ET dynamics. Prior to analysis, both ET and the environment factors were standardized to remove the influence of unit variations on the regression coefficients. Ridge regression analysis was used to assess the effects of each biological and climatic factor on ET, utilizing the flowing formula:

$$X = [NDVI', \quad Pre', \quad RH', \quad Rn', SM', Ta', GW'] \tag{7}$$

$$b = (X^T X + \lambda I)^{-1} X^T ET' \tag{8}$$

ET', NDVI', Pre', RH', Rn', SM', Ta' and GW' are the standardized values of ET, NDVI, precipitation, relative humidity, net solar radiation, soil moisture, temperature and groundwater respectively. X is the independent variable matrix, and b refers to the standardized ridge regression coefficient. λ and I denote the regularization parameter and the identity matrix, respectively.

We calculated the relative contributions of these factors to ET variation by using ridge regression coefficients along with the standardized trends of each factor to determine the influence of different climatic elements on ET dynamics:

$$\eta_i = b_i \bullet \quad x_{i\_trend} \tag{9}$$

$$C_i = \frac{|\eta_i|}{|\eta_1| + |\eta_2| + |\eta_3| + |\eta_4| + |\eta_5| + |\eta_6| + |\eta_7|} \tag{10}$$

where x_{i_trend} is the normalized trend of independent variable, C_i denotes the relative contribution of the i-th factor (where $i = 1$–7) to ET variability. This calculation allows us to identify the relative importance of each factor in driving ET changes. A larger C_i value indicates a greater influence of that specific factor on ET fluctuations.

2.5.4. Statistical evaluations

We evaluated the model's accuracy by comparing its predicted ET_a with observations from flux towers using a suite of commonly applied statistical metrics. These indicators were selected to assess model efficiency and quantify prediction error, which include: (1) Goodness-of-fit and model efficiency indicators: the coefficient of determination (R^2) and the Nash-Sutcliffe Efficiency (NSE); (2) Error-based performance metrics: Root Mean Square Error (RMSE), Mean Bias Error (MBE), Mean Absolute Error (MAE), Mean Absolute Percentage Error (MAPE), and Mean Bias Percentage Error (MBPE). The formulas and definitions of these evaluation metrics are provided in Supplementary Materials (Text S1). These metrics together offer a comprehensive evaluation of model accuracy and robustness across diverse environmental conditions.

3. Results

3.1. Validation of the optimized ET_a model

Fig. 2 displays the validation outcomes of the 8-day average ET_a values simulated by the PT-JPL model, both before and after parameters optimization, compared to the observed ET_a data. In general, the PT-JPL showed a reliable performance using the default parameter settings. However, the overall performance of the model showed significant improved performances after model optimization. The R^2 and NSE increased from 0.68 to 0.74 (an increase of 8.8 %) and 0.62–0.68 (an increase of 9.7 %), respectively, while the RMSE, MAE, and MBE decreased from 0.95 to 0.87 mm/day (a decrease of 8.4 %), 0.62–0.53 mm/day (a decrease of 14.5 %), and −0.34 to −0.37 mm/day, respectively. Since MBE is a signed metric, although its absolute value slightly increased after optimization, the overall bias remained within an acceptable range. Overall, the MAPE and MBPE across all sites are 14.4 % and −10.1 %, respectively.

Furthermore, site-specific validation across different vegetation types (Supplementary Fig. S2) confirmed the robustness of the optimized model. The highest simulation accuracy was observed in grassland (R^2 = 0.87; NSE = 0.84), followed by shrubland, forestland, and desert ecosystems, which also exhibited low RMSE and MBE values. In contrast, performance in wetland areas was relatively weaker, with wetland showing the lowest R^2 (0.61) and the highest RMSE (1.59 mm/day). These results suggest that the optimized PT-JPL model performs best in ecosystems with simpler vegetation structures and more stable surface conditions.

3.2. Spatiotemporal variations of ET_a

Fig. 3 illustrates the annual and seasonal variations in ET_a across NWC from 2001 to 2024. During this period, the annual average ET_a showed a slight increasing trend, with a rate of 0.43 mm/year and a determination coefficient (R^2) of 0.32. Specifically, ET_a increased from 297.5 mm in 2001–330.6 mm in 2024, representing a total growth of 11.1 % over the 24-year span. Seasonal patterns of ET_a demonstrated noticeable differences. In summer, ET_a showed an increasing trend of 0.78 mm/year, with a mean value of 146.6 mm over the study period. In winter, ET_a also increased, albeit more modestly, at a rate of 0.01 mm/year, with a mean of approximately 1 mm. Conversely, spring ET_a exhibited a slight decreasing trend of 0.22 mm/year, with a mean value

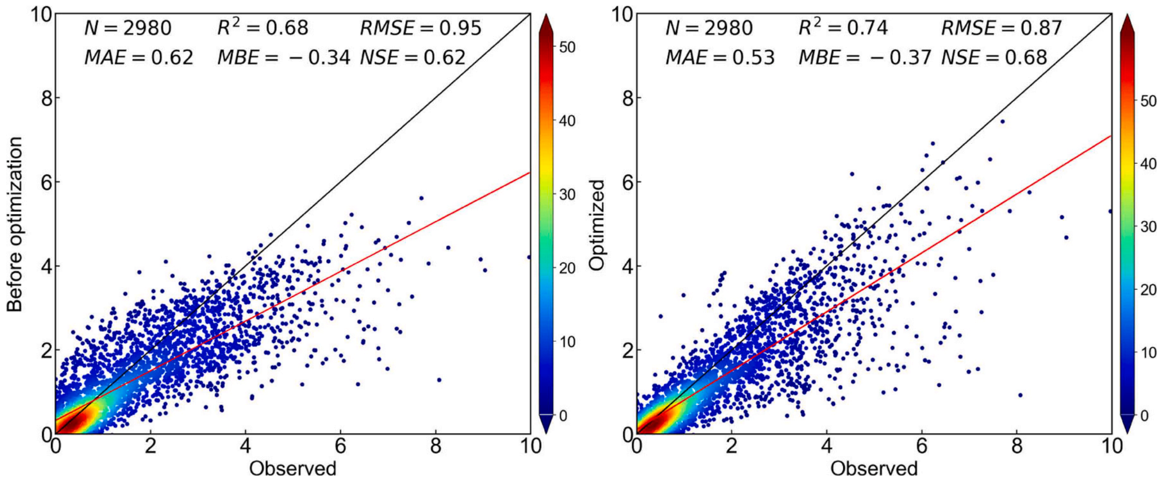

Fig. 2. Scatterplots between observed ET_a (mm/day) and simulated ET_a with all flux site data by PT-JPL before and after optimization. The black lines represent the 1:1 lines, while the red lines indicate the linear regression results. The units for RMSE, MAE, and MBE were mm/day.

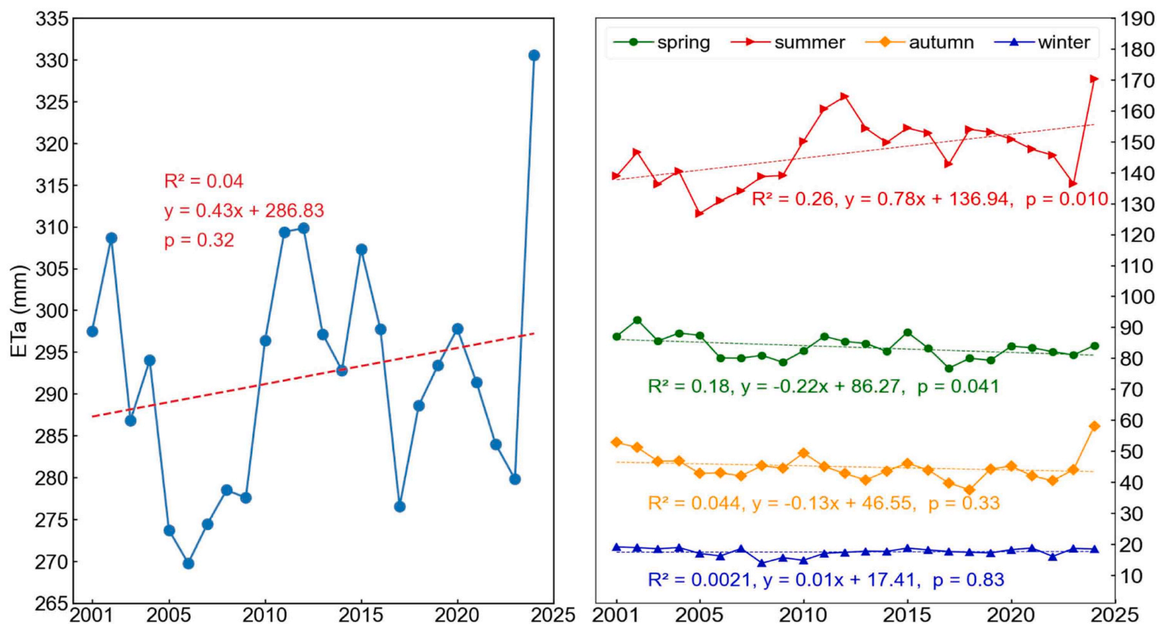

Fig. 3. The temporal variations of spatially averaged annual and seasonal ET_a in Northwest China from 2001 to 2024.

of 83.5 mm. Similarly, in autumn, ET_a decreased at a rate of 0.13 mm/year, with an average of 44.9 mm. These findings indicate that while the overall ET_a in the region experienced a gradual upward trend, the seasonal dynamics varied, with increasing trends in summer and winter and decreasing trends in spring and autumn.

Fig. 4 illustrates the spatial distribution of the multi-year average ET_a and its long-term trend across NWC from 2001 to 2024. During this period, the annual average ET_a ranged from 0 to 843.4 mm, with a

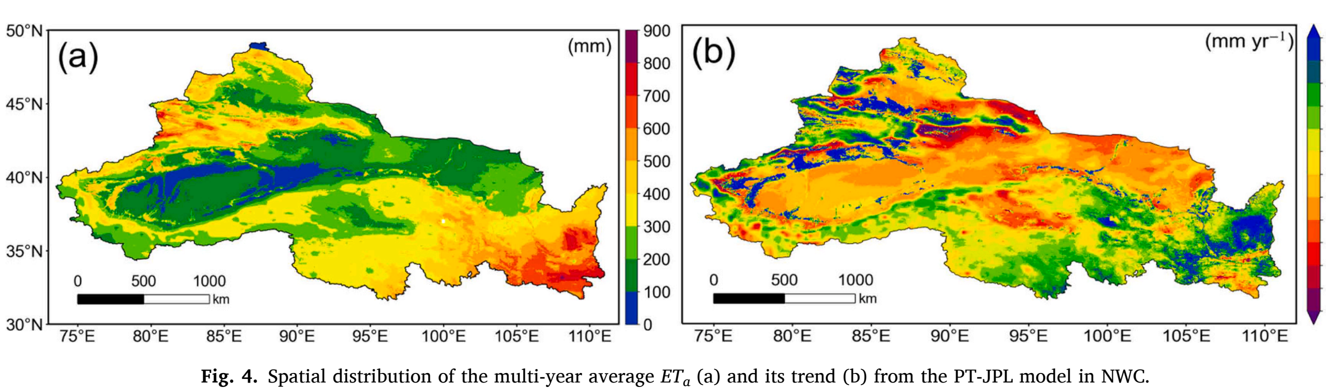

Fig. 4. Spatial distribution of the multi-year average ET_a (a) and its trend (b) from the PT-JPL model in NWC.

regional multi-year mean of 292.2 mm. ET_a shows a distinct east-west gradient, with higher values in the eastern regions and lower values in the west. The majority of the areas experienced no significant change in ET_a. Specifically, only 13.9 % of the regions exhibited a highly significant increase in ET_a, 9.2 % showed a slight increase, 26.2 % showed no significant change, and 50.7 % experienced a decrease in ET_a values, with 20.1 % and 7.9 % showing highly significant and slightly significant decreases, respectively. The spatial distribution of ET_a trends revealed notable regional heterogeneity. Significant increases in annual ET_a ($p < 0.01$) were mainly concentrated in ecologically restored and vegetated zones of the southeastern region such as parts of the Loess Plateau, as well as in oasis zones surrounding desert margins in the northwestern region. In contrast, the central and western arid zones, particularly those with sparse vegetation or shifting land cover, exhibited minimal or slightly declining ET_a trends. These patterns underscore the combined effects of ecological restoration, land use change, and climatic variability on ET_a dynamics across dryland environments. Seasonal comparisons of ET_a (Supplementary Fig. S3) indicate that evapotranspiration from annual vegetation is predominantly concentrated in spring and summer, with minimal ET_a observed during autumn and winter.

3.3. Impacts of vegetation dynamics and climate factors on ET_a dynamics

Fig. 5 presents the spatial patterns of partial correlation coefficients between ET_a and seven driving factors. NDVI shows a strong positive partial correlation with ET_a in 97.6 % of vegetated areas, with negative coefficients (2.4 %) primarily on the Tibetan Plateau (Fig. 5a). Precipitation exhibits a predominantly positive correlation (64.6 %), with weak negative zones (35.4 %) in the central and eastern part of NWC (Fig. 5b). Relative humidity positive correlates with ET_a in 99.3 % of the region, particularly in arid zones, while negative effects are limited to eastern part of NWC (Fig. 5c). Net radiation shows the highest consistency, with 99.9 % of the region exhibiting strong positive correlation (Fig. 5d). Soil

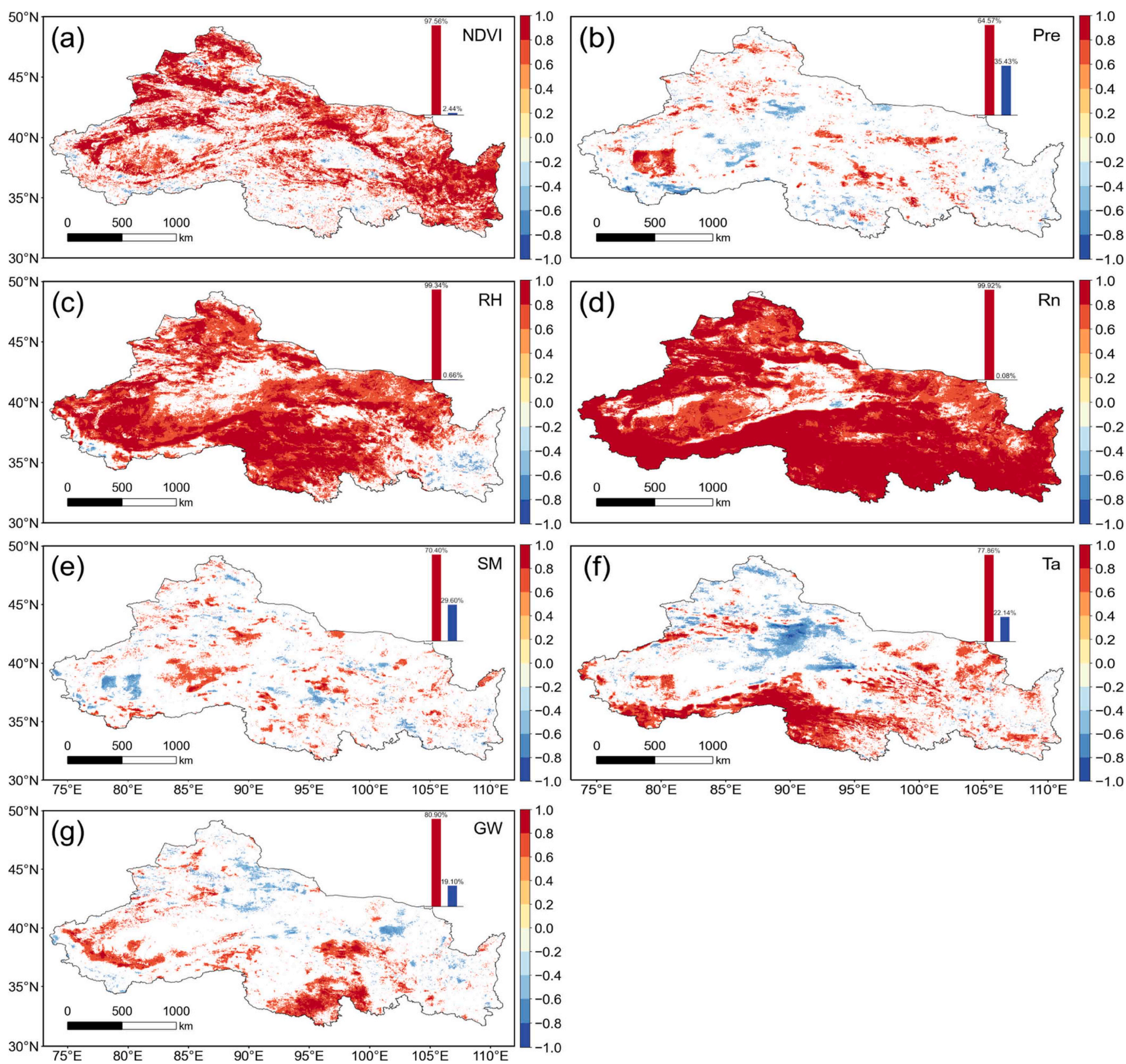

Fig. 5. Partial correlation coefficients between each factor and interannual ET_a during the study period, with statistically significant at $p < 0.05$.

moisture has a mixed impact, with 70.4 % positive and 29.6 % negative correlations, distributed irregularly (Fig. 5e). Air temperature positively affects 77.9 % of the region, mainly in highlands, while 22.1 % shows negative correlation, especially in central deserts (Fig. 5f). Groundwater shows a strong positive influence in 80.9 % of the region, especially in the oases of the Tarim Basin and the southern QTP (Fig. 5g).

3.4. Contributions of environmental factors and vegetation dynamics to ET_a variability

We assessed the relative influences of vegetation dynamics and climatic factors on ET_a variability in NWC by using the ridge regression (Fig. 6). Overall, both sets of factors significantly impacted ET_a changes, with NDVI playing a dominant role in most of the vegetation zones in NWC, including the Qinling region, the Loess Plateau, the Tianshan region, the Circum-Taklamakan Desert oasis zone, and parts of the Tibetan Plateau. In contrast, precipitation had a significantly weaker influence, playing the dominant role only in the Jungar Basin and small parts of the Tibetan Plateau. In the north-central section of the region, which includes numerous deserts, relative humidity emerged as the primary factor, suggesting that humidity plays a vital role in influencing ET_a within hyper-arid zones. In northwestern China, the dominant role of net radiation was correlated with altitude, being particularly influential in the Tien Shan Mountains, the Kunlun Mountains, the Altun Mountains, the Qilian Mountains, and much of the Tibetan Plateau. Similarly, the contribution of air temperature to ET_a variation is associated with elevation. Fig. 6f illustrates that air temperature has a relatively higher contribution in the Tibetan Plateau, while its impact is less significant in low-elevation areas. In the northwestern part of NWC and the central-southern QTP, the changes in groundwater contribute significantly to the variation in ET (Fig. 6g).

Fig. 7a depicts the spatial patterns and statistical values of the primary factors driving ET_a variability in NWC. NDVI accounts for 16.6 % of the ETa variation in NWC, with its dominant influence mainly

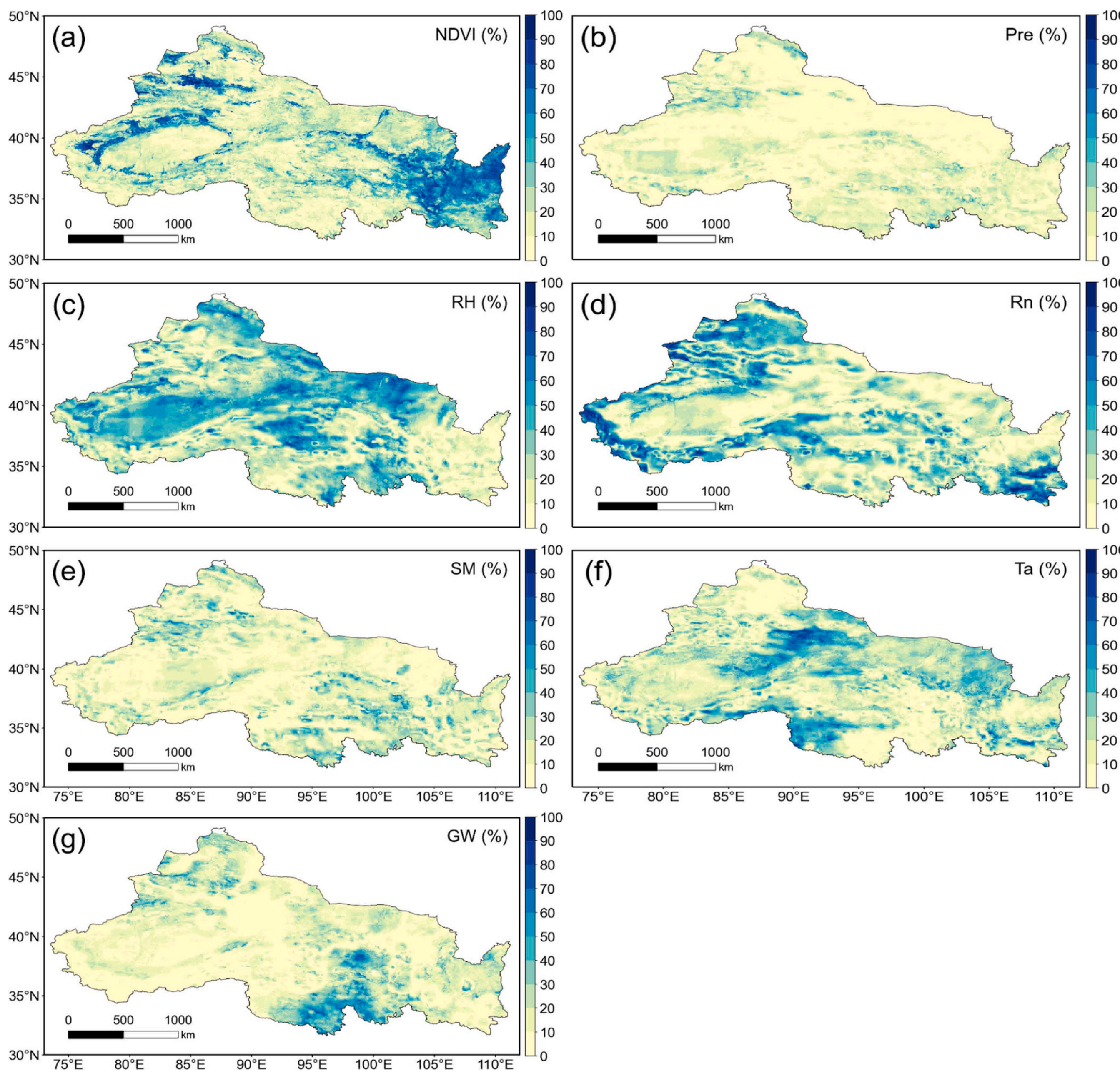

Fig. 6. The relative contributions of the biological (NDVI) and climatic factors (Pre, RH, Rn, SM,Ta and GWD) to interannual ET_a during the study period.

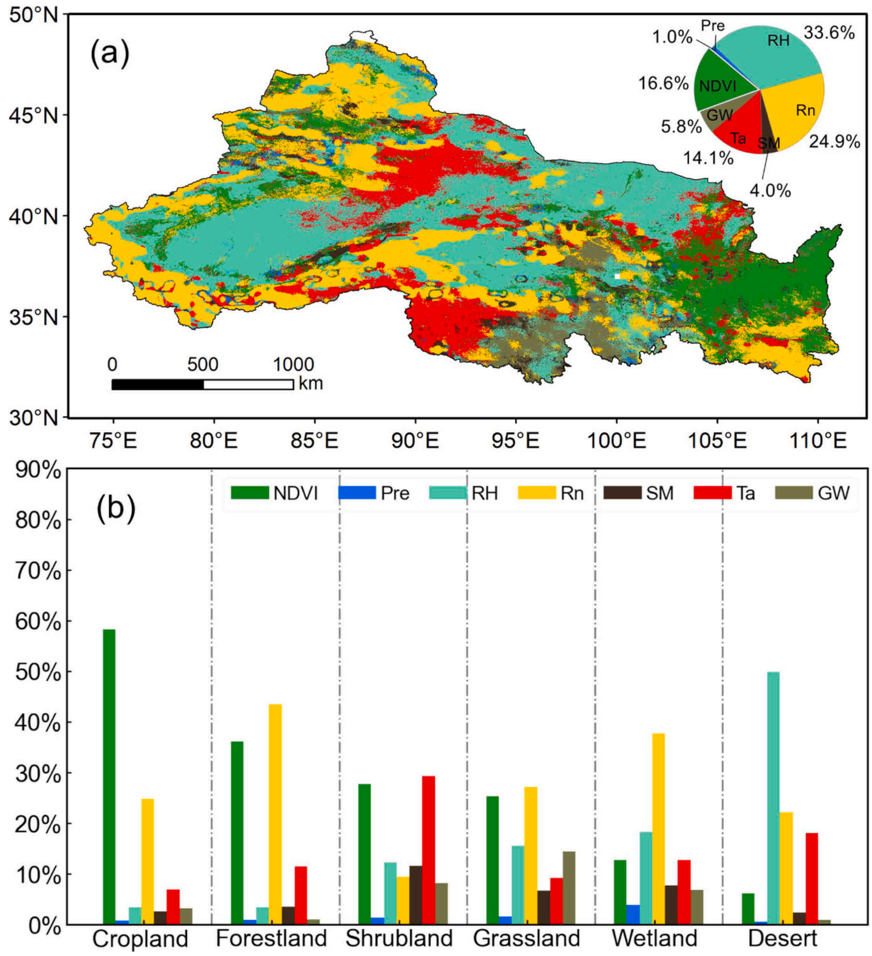

Fig. 7. Distribution of the dominant factors in ETa changes of the region (a) and contribution of the dominant factors influencing evapotranspiration in different land cover types (b).

concentrated in the southeastern region and the oasis areas surrounding the Tarim Basin. Climate factors were also significant, with precipitation affecting ET_a across 1.0 % of the study area, particularly in parts of the Junggar Basin, Taklimakan Desert, and small portions of the QTP. Relative humidity was the dominant factor in desert and desertified areas, covering 33.6 % of the entire region. In high-altitude areas, net radiation governed ET_a changes over 24.9 % of the region such as the Tianshan, Kunlun, Altun, Qilian Mountains and the QTP. Soil moisture accounted for 4.0 % of the variation in ET_a, exhibiting a heterogeneous spatial distribution. Temperature induced ET_a changes in only 14.1 % of the area, primarily affecting the QTP. Groundwater is also an important factor influencing ET_a variation in NWC, affecting 5.8 % of the area, with its dominant influence primarily concentrated the northwestern part of NWC and the central-southern QTP. Overall, climate factors accounted for 83.4 % of ET_a variations, while vegetation factors (NDVI) contributed to 16.6 % of ET_a changes.

Fig. 7b shows the contribution of key factors to ET_a across various vegetation types in NWC. For forestland, NDVI and net radiation were the most influential factors, contributing 36.2 % and 43.5 %, respectively, while other factors each contributed less than 20 %. In cropland, NDVI and net radiation were the primary contributors, accounting for 58.3 % and 24.7 %, respectively. In grasslands, net radiation, NDVI, relative humidity and groundwater were the primary drivers of ET_a changes, with contributions of 27.1 %, 25.3 %,15.6 % and 14.5 %, respectively. For shrublands, temperature was the most influential factor, contributing 29.4 %. And for wetlands, net radiation was the most influential factor, contributing 37.7 %. In desert, the main contributing factors were relative humidity and net radiation, accounting for 49.9 % and 22.1 %, respectively; notably, temperature also played a significant role, contributing 18.0 %. Overall, relative humidity, NDVI, and net radiation emerged as the primary drivers of ET_a variation across most vegetation types, while the influence of other factors was relatively minor.

3.5. Effects of land cover changes on vegetation dynamics and ET_a variations

Building on the attribution results in Section 3.4, which identified vegetation dynamics (NDVI) as a major driver of ET_a variability, this section investigates the land cover transitions that underlie long-term NDVI trends. By linking land use transitions to ecosystem-level ET responses, we aim to better understand the anthropogenic and natural processes behind long-term ET_a variability in dryland environments. Fig. 8 illustrates the spatial distribution of NDVI trends from 2001 to 2024 (Fig. 8a), their corresponding significance (p-values; Fig. 8b), as well as the correlation coefficients between NDVI and ET_a (Fig. 8c) and their statistical significance (Fig. 8d). The results show that the majority of vegetation-covered areas in NWC experienced a significantly increasing NDVI trend with a regional trend of 0.0011 yr^{-1} (Supplementary Fig. S4). This greening trend is particularly prominent in ecologically restored zones such as the Loess Plateau, Tianshan Mountains, and the oasis regions of southern Xinjiang. These regions exhibited statistically significant greening trends ($p < 0.05$), suggesting ongoing ecological improvement and vegetation recovery. Furthermore, the spatial distribution of NDVI-ET_a correlation coefficients indicates a strong positive relationship between vegetation activity and ET_a,

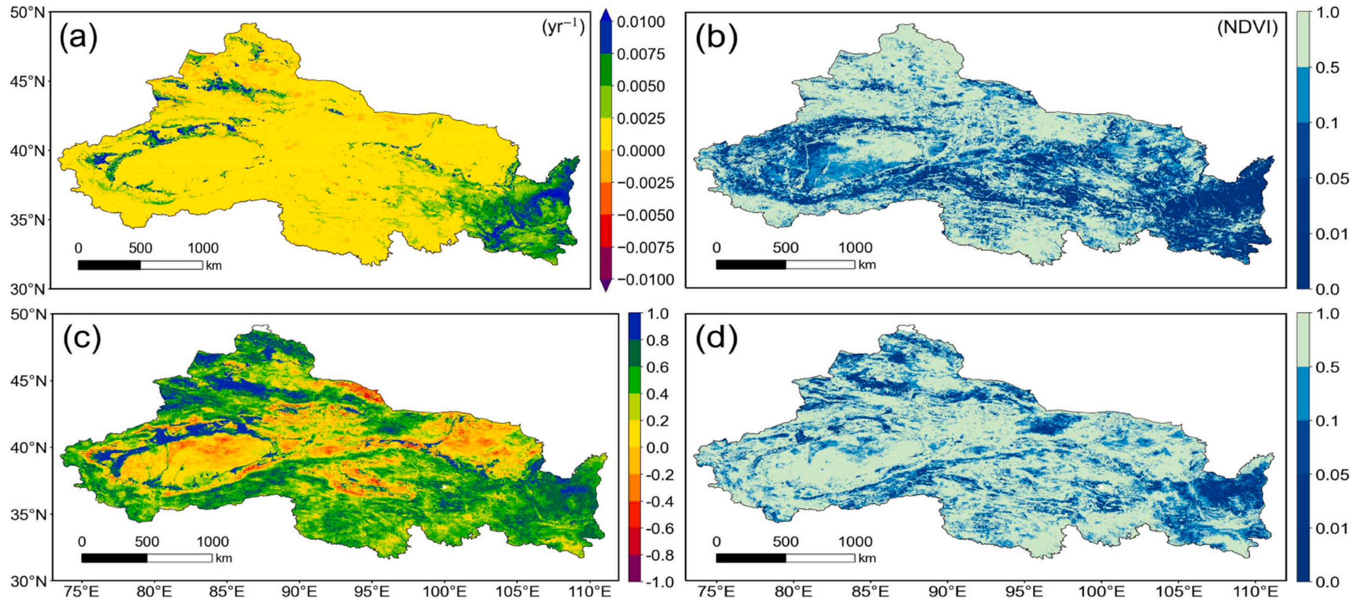

Fig. 8. Spatial distribution of the interannual trends in NDVI (a) and their statistical significance (b), and the correlation coefficients between NDVI and ETa (c) and corresponding significance levels (p-values) (d) from 2001 to 2024.

especially in the eastern and southern parts of the region (Fig. 8c). High correlation values (>0.6) are concentrated in areas with active vegetation restoration or irrigation, such as the Loess Plateau and the Tarim Basin oases, implying that vegetation dynamics play a substantial role in driving ET_a changes in these zones. In contrast, desert regions such as the Junggar Basin and the central Gobi areas show weak or even negative correlations, highlighting the limited coupling between NDVI and ET_a in sparsely vegetated or water-limited landscapes.

As shown in Fig. 9, a clear relationship exists between the area of each land cover type and its corresponding total ET_a. Generally, land types with larger areas, such as forests and croplands, exhibit higher total ET_a values due to their widespread distribution and dense vegetation cover, both of which promote evapotranspiration. Forests and croplands not only experienced notable increases in area during the study period but also showed significant growth in total ET_a, with forestlands increasing by 4.81×10^6 mm/year and croplands by 6.62×10^6 mm/year, respectively. This co-evolution suggests that vegetation expansion in these land types has directly contributed to regional increases in ET_a. In contrast, land types with smaller areal extent, such as shrublands and wetlands, showed relatively stable trends in both area and total ET_a, indicating a limited impact on the overall spatiotemporal ET_a dynamics in NWC. These findings reinforce the importance of land use transitions, particularly afforestation and agricultural development, in shaping regional water flux patterns.

Table 3 summarizes the land cover changes in NWC between 2001 and 2024. Over the 24-year period, forestland expanded by 40,698.0 km^2, representing a 54.3 % increase compared to 2001, with grasslands and croplands serving as the primary sources of this growth. Grasslands area increased by 35,983.3 km^2, primarily due to the conversion of desert areas, along with some croplands transitioning to grasslands. Meanwhile, cropland area increased by 66,852.3 km^2, predominantly through the conversion of grasslands and desert into cropland. Although there was mutual conversion between grasslands and croplands, the net flow favored cropland expansion, indicating an overall trend toward agricultural intensification. Additionally, desert area experienced the largest reduction, shrinking by 136,277.2 km^2, most of which was transformed into grasslands. This substantial decline highlights the effectiveness of desertification control initiatives, such as ecological restoration and vegetation rehabilitation projects. The observed land cover transitions reflect both ecological improvement and human land use pressures. While programs like the "Grain for Green" initiative have contributed positively to forest and grassland recovery, the concurrent expansion of cropland—often at the expense of grasslands—underscores a potential trade-off between agricultural development and ecological restoration goals.

Fig. 10 shows the spatial distribution of land cover conversions across NWC between 2001 and 2024. Land cover changes were primarily concentrated in grasslands, croplands, and forestlands. During this 24-year period, grasslands and croplands areas exhibited substantial expansion, with 50.2 % of current grasslands and 25.0 % of croplands converted from other types. The expansion of grasslands and croplands was primarily concentrated in ecologically sensitive or restored zones, including the Loess Plateau, Turpan-Hami Basin, QTP, Tianshan Mountains, and the oases of the Tarim Basin. Additionally, forestlands area also increased by 10.7 %, mainly in the Loess Plateau, reflecting the impact of large-scale ecological restoration projects. These spatial patterns of land conversion were broadly consistent with areas showing significant increases in ET_a and NDVI, suggesting that land use change—particularly afforestation and agricultural expansion—has played a key role in driving evapotranspiration dynamics. To better capture cropland dynamics, we analyzed cropland-specific changes from 2001 to 2024 (Supplementary Fig. S5). The results show that 49.1 % of cropland (131,318.5 km^2) remained unchanged, while 13.0 % (34,631 km^2) was lost and 38.0 % (101,483.3 km^2) represented newly added cropland, resulting in a total cropland area of 232,801.8 km^2 in 2024. These changes were mainly concentrated in localized oasis regions such as the Hexi Corridor and southern Xinjiang, suggesting that although cropland underwent substantial local expansion or reallocation, the overall regional extent remained relatively stable.

Fig. 11 illustrates the changes in NDVI and ET_a associated with land use conversion between 2001 and 2024. As shown in Fig. 11a, average NDVI values increased across all land use types that underwent conversion, except for desert areas. The most pronounced increase was observed in forestlands, with NDVI rising by 0.1337 (26.9 %). Croplands and grasslands also experienced substantial increases of 0.1233 (50.6 %) and 0.0556 (38.5 %), respectively. These results indicate that vegetation greening accompanied most land cover transitions. Fig. 11b displays the corresponding changes in total ET_a for these converted areas. Croplands exhibited the largest absolute increase in ET_a, with a rise of 7.23×10^7 mm (43.5 %) in 2024 compared to 2001. Moreover, grasslands and

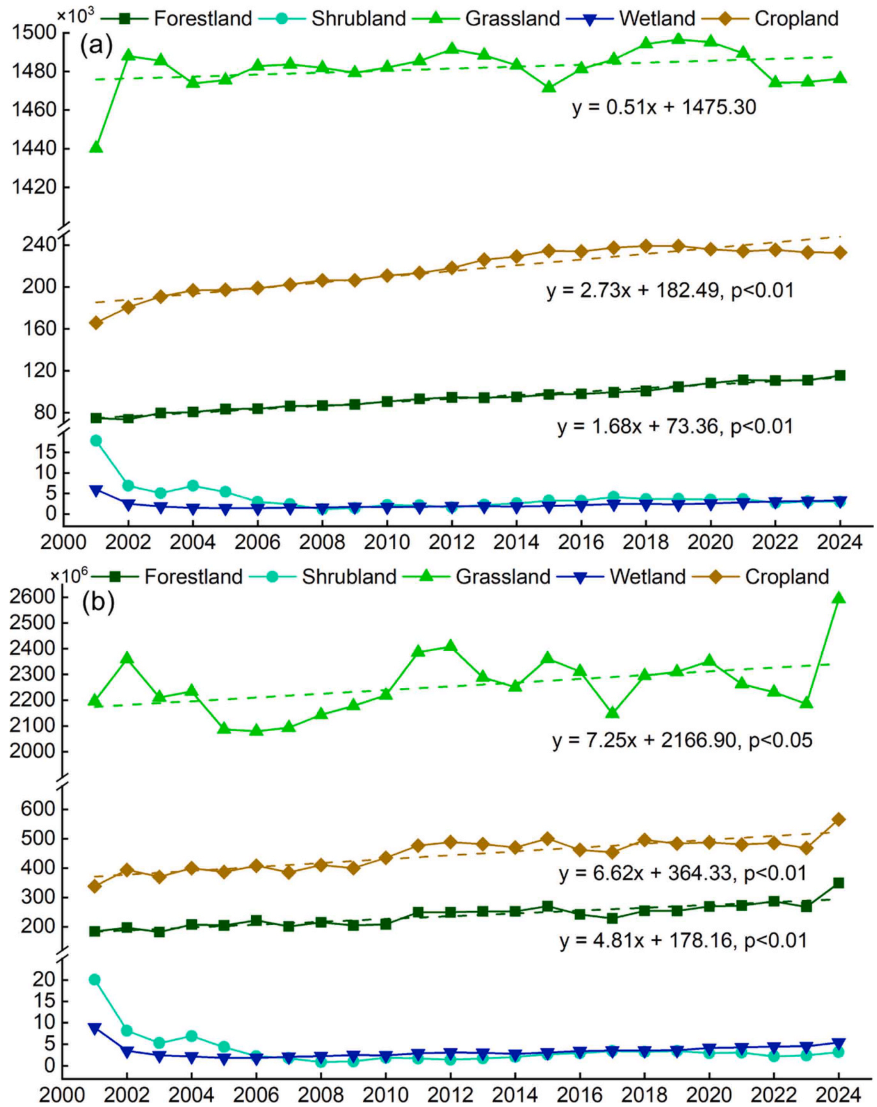

Fig. 9. Interannual variation of cumulative annual land cover area (a) and annual ET_a (b) for different land types in NWC.

Table 3
The land cover type transition matrix in Northwest China from 2001 to 2024 (units: km^2).

2024 / 2001	Forestland	Shrubland	Grassland	Wetland	Cropland	Desert	Others	Total (2001)
Forestland	72148.8	9.8	2605.5	110.0	19.8	1.0	2.3	74,897.0
Shrubland	38.3	479.0	16234.3	0.0	308.5	736.5	57.0	17853.5
Grassland	35417.0	678.3	1272,110.5	821.0	95,519.8	35,058.0	650.5	1440,255.0
Wetland	490.5	3.8	3112.5	2042.3	95.5	144.5	106.5	5995.5
Cropland	7500.5	68.0	26573.8	50.3	131,318.5	42.0	396.5	165,949.5
Desert	0.0	1766.5	155,409.8	136.0	5518.3	2279,291.5	13,091.0	2455,213.0
Others	0.0	3.8	192.0	78.0	21.5	3662.3	44,133.0	48,090.5
Total (2024)	115,595.0	3009.0	1476,238.3	3237.5	232,801.8	2318,935.8	58,436.8	4208,254.0

forestlands conversions also led to notable ETa increases of 4.46×10^7 mm (16.9 %) and 3.03×10^7 mm (29.9 %), respectively, suggesting that afforestation projects not only enhanced vegetation cover but also significantly increased water consumption through evapotranspiration.

4. Discussion

4.1. Performance of the improved model and the variations in ET_a

The results indicate that the PT-JPL model effectively simulates ET_a in arid and semi-arid areas. Compared with the uncalibrated version, parameter optimization based on flux tower data significantly improved model performance, particularly across typical vegetation types in NWC. By integrating the model with flux tower dataset, we optimized key sensitivity parameters using ET_a observations from different land cover types, which improved the simulation accuracy across varied ecosystems. Compared to other models (Ershadi et al., 2014; Fisher et al., 2008), our calibrated PT-JPL framework achieved improved accuracy in grassland, shrubland, and desert regions, as evidenced by a relatively lower RMSE in these ecosystems. These improvements stem largely from

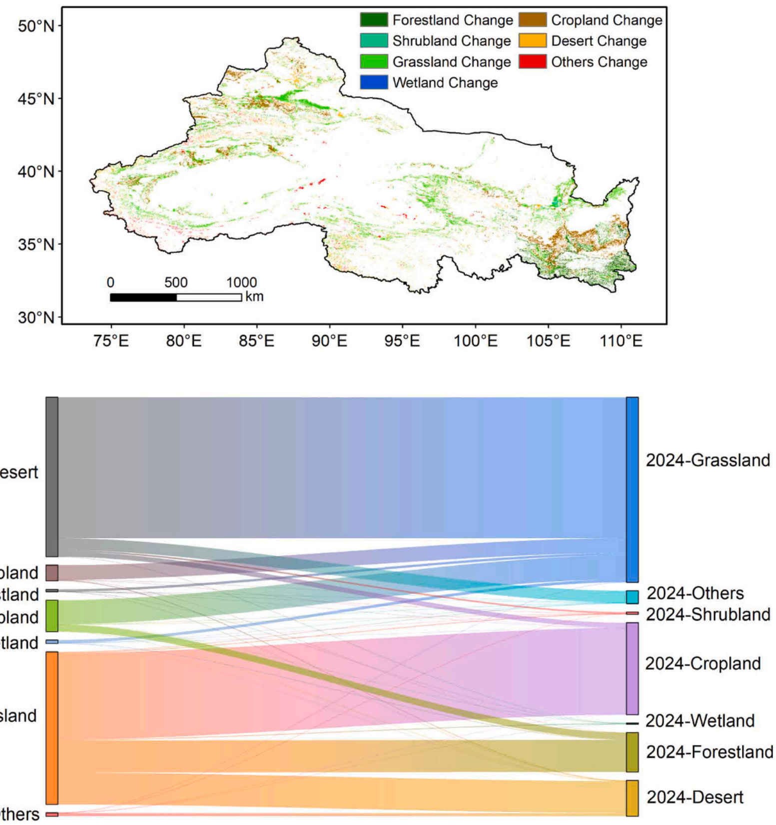

Fig. 10. (Top) Spatial distribution of land cover changes in Northwest China from 2001 to 2024. (Bottom) Sankey diagram illustrating the type transitions of land cover during the same period.

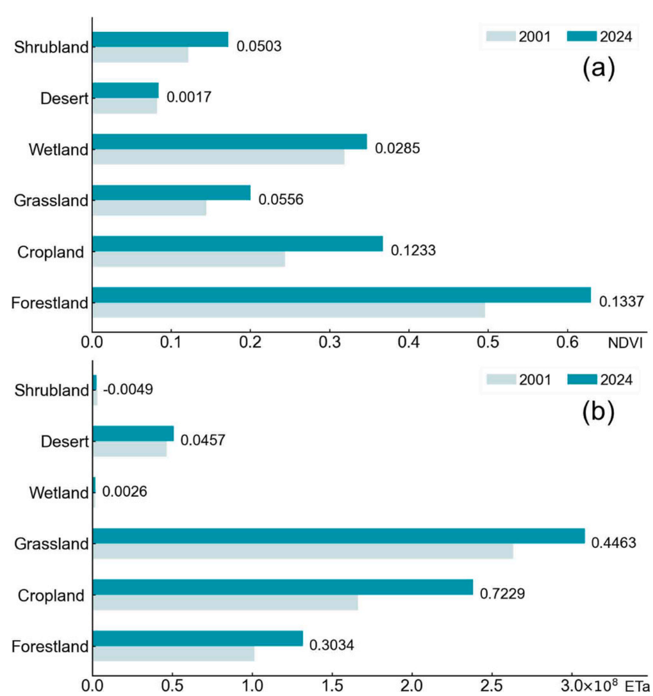

Fig. 11. Changes in mean NDVI (a) and total annual ET_a (b) in areas with land use conversion, showing the difference between 2024 and 2001.

reduced vegetation heterogeneity and more stable environmental conditions in these ecosystems, which allow the model's simplified structure to perform well. In contrast, accuracy was lower for cropland, forestland, and wetland areas due to their structural complexity and high spatial variability in soil and vegetation characteristics.

To further assess model performance, we compared the PT-JPL ETa estimates with two widely used satellite-based ET products—MODIS MOD16A2 (Mu et al., 2011) and PML-V2 (Zhang et al., 2019)—using the same flux tower observations as reference (Supplementary Figs. S6-S7). The PT-JPL dataset showed superior accuracy, with a mean R^2 of 0.74 and RMSE of 0.87 mm/day. PML-V2 yielded moderate agreement ($R^2 =$ 0.59, RMSE = 1.05 mm/day), but exhibited larger errors in forest and wetland areas. MOD16A2 performed the least reliably ($R^2 = 0.31$, RMSE = 1.34 mm/day), with systematic underestimation in sparsely vegetated and hydrologically complex regions. These results highlight the advantages of the parameter-optimized PT-JPL model in capturing ETa dynamics across heterogeneous dryland ecosystems.

The spatial distribution of ET_a values in our results reveals that the northwest and southeast subregions show relatively high ET_a values, while the central desert zones exhibit lower values, consistent with earlier studies (Yang et al., 2022). The PT-JPT model performs particularly well in regions with simpler vegetation structures, though it still underestimates ET_a where soil evaporation dominates, especially in highly heterogeneous cropland and wetland systems. From 2001–2024, ET_a in NWC exhibited a modest increasing trend of 0.43 mm/year, consistent with previous studies (Li et al., 2022). Although the overall performance of the PT-JPL model is robust, there remains room for further improvements, particularly in better representing soil evaporation and complex land cover types. Our findings support the suitability of the PT-JPL model, especially when optimized with EC observations, for long-term ETa simulation in data-scarce, environmentally complex drylands.

4.2. Statistical attributions of ET_a variability to vegetation and environmental factors

ET variability in arid regions is influenced by multiple interacting drivers, including vegetation dynamics, climatic conditions, and water availability (Chen et al., 2018; Yang et al., 2022). In this study, we analyzed six major climatic factors, precipitation, relative humidity, net radiation, soil moisture, air temperature and groundwater, alongside NDVI to identify their relative contributions to ET_a in the dryland environments of NWC. Vegetation dynamics, represented by NDVI, is an key driver of ET_a variation in vegetated zones (Yang et al., 2022; Zheng et al., 2022). As illustrated in Fig. 7, vegetation dynamics exhibits strong positive partial correlations with ETa in most vegetation-rich areas, reflecting the dominant role of transpiration in dryland regions, where a significant portion of ET_a is derived from vegetation transpiration, while soil evaporation constitutes a considerably smaller fraction (Zhang et al., 2020).

However, the ridge regression results indicate that climatic drivers overall explain a greater proportion (83.38 %) of ET_a variability compared to vegetation dynamics (16.62 %). Among the climatic factors, relative humidity (33.64 %), net radiation (24.87 %) and temperature (14.10 %) are the most influential. This highlights the critical role of water availability and energy input in controlling ET_a under arid conditions. In high-altitude regions such as Qinghai-Tibetan Plateau, net radiation and air temperature exert stronger control on ET_a due to elevation-related energy limitations (Ma et al., 2019). For example, increased ET_a may lead to enhanced water vapor and local cooling, which subsequently suppress radiation (Yu et al., 2022), reinforcing the need to consider regional energy-water feedbacks.

Our results also confirm that water-related variables, especially groundwater, relative humidity, and soil moisture, are key determinants of ET_a in arid zones. This aligns with prior findings that relative humidity governs ET_a variations in water-scarce regions (Chen et al., 2014; Li et al., 2021; Yang et al., 2022). This also aligns with the complementary relationship (CR) theory (Brutsaert and Stricker, 1979), which suggests that in moisture-limited environments, increases in potential evapotranspiration (ET_o) may not translate to higher ET_a due to low soil moisture availability and soil-atmosphere feedbacks (Wang and Zlotnik, 2012). Our supplementary analysis (Supplementary Fig. S8) confirms that *ETo* trends do not always track *ETa* in arid ecosystems.

Notably, precipitation had a negligible impact on ET_a variation in NWC, accounting for only 1.0 %. This may be attributed to the fact that, in extremely arid regions, the precipitation contributes little directly to ET_a, but indirectly affects it via subsurface water. By contrast, groundwater and irrigation provide more stable and sustained sources of moisture, particularly for oases and riparian ecosystems (Wang et al., 2023, 2021). Therefore, in extremely arid areas with limited precipitation, water availability from irrigation or atmospheric moisture, rather than precipitation, dominates ETa dynamics.

4.3. Land cover change impacts on ETa and implications of afforestation and agricultural expansion

While statistical attribution identifies dominant variables, understanding their ecological and land-use origins requires spatial interpretation of vegetation change. Our study demonstrates that areas with significantly increasing ET_a and NDVI are often associated with land cover transitions, particularly afforestation and farmland expansion. In regions such as the Loess Plateau, NDVI increased by 0.0010 unit/year, coinciding with a 0.43 mm/year increase in ET_a. These changes indicate enhanced transpiration from newly established vegetation, particularly under ecological restoration programs like the “Grain for Green” project (Li et al., 2022; Shao et al., 2019).

Additionally, forestland area increased by 40,698.0 km^2 (54.3 %) from 2001 to 2024, primarily through conversion from croplands and grasslands, particularly in the Loess Plateau. While these changes enhance vegetation cover (increases of 26.9 % for forests and 38.5 % for grasslands), they also contributed to ET_a increases of 29.9 % and 16.9 %, respectively. This trade-off between ecological restoration and water use must be carefully managed (Li et al., 2022). Similarly, cropland expansion in the Hexi Corridor and southern Xinjiang has raised water demand, contributing to increased ET_a and NDVI (Yang et al., 2023). Although cropland and grassland expansion enhances vegetation productivity (Liu et al., 2024), it also intensifies the tension between ecological restoration and agriculture water use (Ren et al., 2022), especially when grasslands are converted to irrigation-dependent croplands. Overall, our findings highlight the dual effects of land greening policies: while improving ecological benefits, they elevate regional water consumption. This dual effect underscores the need for integrated water and land management strategies. Therefore, sustainable development in NWC requires integrated land-water planning that considers both environmental and hydrological trade-offs.

4.4. Uncertainties and limitations

In this study, MODIS remote sensing data and bilinearly interpolated GLDAS meteorological data were employed to drive the PT-JPL model. While spatial resolution was harmonized to 500 m, the interpolation process may have smoothed local climatic variability, potentially introducing biases in ET_a simulation, particularly in regions with complex topography or microclimates. Despite its widespread use and good agreement with ground observations across NWC, GLDAS still exhibits biases in certain meteorological drivers that may lead to uncertainties in ETa simulation, especially in complex or data-scarce regions. In NWC, where vegetation is sparse and soil evaporation constitutes a large portion of total ET, the PT-JPL model tends to underestimate ET_a. This bias is likely stems from the model’s simplified treatment of soil evaporation processes (Cui et al., 2021), which is crucial in arid regions dominated by bare soil and low vegetation cover.

Additionally, the use of MODIS land use classification introduces uncertainty, given its limited accuracy in heterogeneous landscapes. Classification errors may propagate through model parameter assignment and affect final ET_a estimates. These uncertainties could be reduced by incorporating high-resolution or multi-source land cover datasets. Flux tower data availability also constrains parameter optimization. Sparse site distribution, the footprint representativeness and measurement errors of EC observations may introduce uncertainty in regional parameter calibration (Hicks and and Baldocchi, 2020). Therefore, improving the spatial coverage and data quality of flux tower networks, and adopting footprint-aware matching or higher-resolution satellite inputs (e.g., Landsat/Sentinel-2) would further enhance model reliability.

Moreover, interactions between vegetation dynamics and climate variability create attribution challenges (Zhang et al., 2019). Vegetation change can influence ET_a by modifying canopy interception, transpiration rates, and soil evaporation, while climate variability simultaneously alters vegetation growth through shifts in temperature, precipitation, and radiation (Piao et al., 2019; Zhu et al., 2025). These processes from feedback loops: in wet years, enhanced vegetation increases transpiration and local cooling, possibly boosting precipitation (Bonan, 2008; Lee et al., 2011); In dry years, vegetation decline leads to increased soil evaporation and reduced transpiration, amplifying drought (Seneviratne et al., 2010). Disentangling these bidirectional influences is inherently difficult. We used ridge regression to quantify the contribution of each driver to $ET_{a.}$ Although this method mitigates multicollinearity, its inherent bias may lead to inaccuracies in estimating the true effect of individual factors (Zhao et al., 2023). Further research is needed to enhance model structure, improve soil evaporation estimation, refine land cover classification and meteorological inputs, and employ more robust statistical methods to reduce uncertainties in ET_a attribution.

5. Conclusions

This study investigated the spatiotemporal dynamics of ET_a in NWC from 2001 to 2024 using a PT-JPL model optimized with EC flux observations. By integrating multi-source remote sensing and meteorological data, we mapped long-term ET_a trends and quantified the relative contributions of vegetation dynamics, climatic variables, and water-related variables using ridge regression. Our results highlight that water availability (e.g., atmospheric moisture), vegetation dynamics and radiation are the dominant climatic and hydrological factors regulating ETa variability in fragile dryland ecosystems. Vegetation dynamics were found to be the primary driver of ET_a in densely vegetated areas, while water availability (e.g., relative humidity, soil moisture, and groundwater) is the most widespread factor affecting ET_a changes in sparsely vegetated or desert regions. The contribution of radiation to ET_a is related to elevation. In high-elevation zones such as the Tibetan Plateau, temperature exerted a stronger influence on ET_a. We also observed that land cover transformation, particularly afforestation and farmland expansion, significantly contribute to ET_a increases by altering vegetation cover and water use patterns. This study improves our understanding of the mechanisms driving evapotranspiration in dryland environments, offering a scientific basis for future water resource management and ecological planning under climate change. Future research should further refine ET models in heterogeneous landscapes and explore the long-term impacts of projected climate change on evapotranspiration to facilitate sustainable water resource management in NWC and other drylands globally

CRediT authorship contribution statement

Kun Zhang: Writing – review & editing, Resources, Methodology. **Jingfeng Xiao:** Writing – review & editing, Methodology. **Kaixuan Liu:** Writing – original draft, Software, Methodology, Investigation. **Yi Song:** Resources, Data curation. **Yi'na Hu:** Resources, Methodology, Funding acquisition. **Xufeng Wang:** Resources, Methodology, Formal analysis. **Gaofeng Zhu:** Software, Methodology. **Haibo Wang:** Writing – review & editing, Writing – original draft, Supervision, Investigation, Formal analysis, Conceptualization. **Liying Geng:** Resources, Data curation. **Junlei Tan:** Resources, Data curation.

Declaration of Competing Interest

The authors declare that they have no relevant relationships with others that can inappropriately influence this work.

Acknowledgments

This study was funded by the National Key Research and Development Program of China (2023YFF1304700). We would like to express our gratitude for the data shared by the PIs of ChinaFLUX, HiWATER, COIRAS, and the other sites in the National Ecosystem Science Data Center. Jingfeng Xiao was supported by University of New Hampshire via bridge support. We also appreciated the constructive comments from the reviews and editors. The ET dataset for arid Northwest China has been deposited at figshare with a permanent DOI: https://doi.org/10.6084/m9.figshare.30186064.v2.

Appendix A. Supporting information

Supplementary data associated with this article can be found in the online version at doi:10.1016/j.agwat.2025.109941.

Data availability

I have shared the link of my data at figshare with a permanent DOI: https://doi.org/10.6084/m9.figshare.30186064.v1.

References

Allen, R.G., Tasumi, M., Trezza, R., 2007. Satellite-based energy balance for mapping evapotranspiration with internalized calibration (METRIC)—Model. J. Irrig. Drain. Eng. 133, 380–394. https://doi.org/10.1061/(ASCE)0733-9437(2007)133:4(380).

Allen, R.G., Pereira, L.S., Howell, T.A., Jensen, M.E., 2011. Evapotranspiration information reporting: I. Factors governing measurement accuracy. Agric. Water Manag. 98, 899–920. https://doi.org/10.1016/j.agwat.2010.12.015.

Bastiaanssen, W.G.M., Menenti, M., Feddes, R.A., Holtslag, A.A.M., 1998. A remote sensing surface energy balance algorithm for land (SEBAL): 1. Formulation. J. Hydrol. 212–213, 198–212. https://doi.org/10.1016/S0022-1694(98)00253-4.

Beer, 1852. Bestimmung der Absorption des rothen Lichts in farbigen Flüssigkeiten. Ann. Phys. 162, 78–88. https://doi.org/10.1002/andp.18521620505.

Bonan, G.B., 2008. Forests and climate change: forcings, feedbacks, and the climate benefits of forests, 320.

Braak, C.J.F.T., 2006. A Markov Chain Monte Carlo version of the genetic algorithm differential evolution: easy Bayesian computing for real parameter spaces. Stat. Comput. 16, 239–249. https://doi.org/10.1007/s11222-006-8769-1.

Braswell, B.H., Sacks, W.J., Linder, E., Schimel, D.S., 2005. Estimating diurnal to annual ecosystem parameters by synthesis of a carbon flux model with eddy covariance net ecosystem exchange observations. Glob. Change Biol. 11, 335–355. https://doi.org/10.1111/j.1365-2486.2005.00897.x.

Brutsaert, W., Stricker, H., 1979. An advection-aridity approach to estimate actual regional evapotranspiration. Water Resour. Res. 15 (2), 443–450. https://doi.org/10.1029/WR015i002p00443.

Chai, X., He, Y., Shi, P., Zhang, X., Niu, B., Zhang, L., Chen, Z., 2021. An observation dataset of carbon and water fluxes over alpine meadow in Damxung (2004–2010). China Sci. Data 6, 70–79. https://doi.org/10.11922/csdata.2020.0026.zh.

Chen, Y., Xia, J., Liang, S., Feng, J., Fisher, J.B., Li, Xin, Li, Xianglan, Liu, S., Ma, Z., Miyata, A., Mu, Q., Sun, L., Tang, J., Wang, K., Wen, J., Xue, Y., Yu, G., Zha, T., Zhang, L., Zhang, Q., Zhao, T., Zhao, L., Yuan, W., 2014. Comparison of satellite-based evapotranspiration models over terrestrial ecosystems in China. Remote Sens. Environ. 140, 279–293. https://doi.org/10.1016/j.rse.2013.08.045.

Chen, Y., Li, Z., Fan, Y., Wang, H., Deng, H., 2015. Progress and prospects of climate change impacts on hydrology in the arid region of northwest China. Environ. Res. 139, 11–19. https://doi.org/10.1016/j.envres.2014.12.029.

Chen, Y., Xue, Y., Hu, Y., 2018. How multiple factors control evapotranspiration in North America evergreen needleleaf forests. Sci. Total Environ. 622–623, 1217–1224. https://doi.org/10.1016/j.scitotenv.2017.12.038.

Chi, H., Wu, Y., Zheng, H., Zhang, B., Sun, Z., Yan, J., Ren, Y., Guo, L., 2023. Spatial patterns of climate change and associated climate hazards in Northwest China. Sci. Rep. 13, 10418. https://doi.org/10.1038/s41598-023-37349-w.

Cui, Y., Song, L., Fan, W., 2021. Generation of spatio-temporally continuous evapotranspiration and its components by coupling a two-source energy balance model and a deep neural network over the Heihe River Basin. J. Hydrol. 597, 126176. https://doi.org/10.1016/j.jhydrol.2021.126176.

Denmead, O.T., Millar, B.D., 1976. Field Studies of the conductance of wheat leaves and transpiration. Agron. J. 68, 307–311. https://doi.org/10.2134/agronj1976.00021962006800020026x.

Ershadi, A., McCabe, M.F., Evans, J.P., Chaney, N.W., Wood, E.F., 2014. Multi-site evaluation of terrestrial evaporation models using FLUXNET data. Agric. For. Meteor. 187, 46–61. https://doi.org/10.1016/j.agrformet.2013.11.008.

Fisher, J.B., Tu, K.P., Baldocchi, D.D., 2008. Global estimates of the land–atmosphere water flux based on monthly AVHRR and ISLSCP-II data, validated at 16 FLUXNET sites. Remote Sens. Environ. 112, 901–919. https://doi.org/10.1016/j.rse.2007.06.025.

Foken, T., Göckede, M., Mauder, M., Mahrt, L., Amiro, B., Munger, J.W., 2004. Post-field data quality control. In: Lee, X., Massman, W.J., Law, B.E. (Eds.), Handbook of Micrometeorology: A Guide for Surface Flux Measurement and Analysis. Springer, Dordrecht, pp. 181–208. https://doi.org/10.1007/1-4020-2265-4_9.

Gao, B., 2000. Quantitative improvement in the estimates of NDVI Values from remotely sensed data by correcting thin cirrus scattering effects. Remote Sens. Environ. 74, 494–502. https://doi.org/10.1016/s0034-4257(00)00141-3.

Gu, Z., Duan, X., Shi, Y., Li, Y., Pan, X., 2018. Spatiotemporal variation in vegetation coverage and its response to climatic factors in the Red River Basin, China. Ecol. Indic. 93, 54–64. https://doi.org/10.1016/j.ecolind.2018.04.033.

Haario, H., Laine, M., Mira, A., Saksman, E., 2006. DRAM: Efficient adaptive MCMC. Stat. Comput. 16, 339–354. https://doi.org/10.1007/s11222-006-9438-0.

Han, C., Mu, Y., Zha, T., Qin, S., Liu, P., Tian, Y., Jia, X., 2023. A dataset of ecosystem flux measurements in a shrubland ecosystem of the Mau Us Desert in Yanchi, Ningxia, China (2012–2016). Chin. J. Plant Ecol. 47, 1322–1332. https://doi.org/10.17521/cjpe.2023.0001.

Hicks, B.B., Baldocchi, D.D., 2020. Measurement of fluxes over land: capabilities, origins, and remaining challenges. Bound. Layer. Meteorol. 177 (2), 365–394.

Hu, Z., Wang, G., Sun, X., Huang, K., Song, C., Li, Y., Sun, S., Sun, J., Lin, S., 2024. Energy partitioning and controlling factors of evapotranspiration in an alpine meadow in the permafrost region of the Qinghai-Tibet Plateau. J. Plant Ecol. 17, rtae002. https://doi.org/10.1093/jpe/rtae002.

Huete, A., Didan, K., Miura, T., Rodriguez, E.P., Gao, X., Ferreira, L.G., 2002. Overview of the radiometric and biophysical performance of the MODIS vegetation indices. Remote Sens. Environ. 83, 195–213. https://doi.org/10.1016/s0034-4257(02)00096-2.

Jasechko, S., Sharp, Z.D., Gibson, J.J., Birks, S.J., Yi, Y., Fawcett, P.J., 2013. Terrestrial water fluxes dominated by transpiration. Nature 496, 347–350. https://doi.org/10.1038/nature11983.

Ji, X., Zhao, Wenzhi, Jin, B., Zhao, L., Zhao, Wenyue, Du, Z., Chen, Z., Zhang, L., 2023. A dataset of water, heat, and carbon fluxes of an oasis agroecosystem in the middle areas of the Hexi Corridor (2012–2015). China Sci. Data 8, 45–54. https://doi.org/10.11922/11-6035.csd.2023.0025.zh.
Katul, G.G., Oren, R., Manzoni, S., Higgins, C., Parlange, M.B., 2012. Evapotranspiration: a process driving mass transport and energy exchange in the soil-plant-atmosphere-climate system, 2011RG000366 Rev. Geophys 50. https://doi.org/10.1029/2011RG000366.
Kustas, W.P., Norman, J.M., 1999. Evaluation of soil and vegetation heat flux predictions using a simple two-source model with radiometric temperatures for partial canopy cover. Agric. For. Meteor. 94, 13–29. https://doi.org/10.1016/S0168-1923(99)00005-2.
Lee, X., Goulden, M.L., Hollinger, D.Y., Barr, A., Black, T.A., Bohrer, G., Bracho, R., Drake, B., Goldstein, A., Gu, L., Katul, G., Kolb, T., Law, B.E., Margolis, H., Meyers, T., Monson, R., Munger, W., Oren, R., Paw U, K.T., Richardson, A.D., Schmid, H.P., Staebler, R., Wofsy, S., Zhao, L., 2011. Observed increase in local cooling effect of deforestation at higher latitudes. Nature 479, 384–387. https://doi.org/10.1038/nature10588.
Li, F., Xiao, J., Chen, J., Ballantyne, A., Jin, K., Li, B., Abraha, M., John, R., 2023. Global water use efficiency saturation due to increased vapor pressure deficit. Science 381 (6658), 672–677. https://doi.org/10.1126/science.adf5041.
Li, M., Yao, J., Guan, J., Zheng, J., 2021. Observed changes in vapor pressure deficit suggest a systematic drying of the atmosphere in Xinjiang of China. Atmos. Res 248, 105199. https://doi.org/10.1016/j.atmosres.2020.105199.
Li, S., Liang, W., Fu, B., Lü, Y., Fu, S., Wang, S., Su, H., 2016. Vegetation changes in recent large-scale ecological restoration projects and subsequent impact on water resources in China's Loess Plateau. Sci. Total Environ. 569–570, 1032–1039. https://doi.org/10.1016/j.scitotenv.2016.06.141.
Li, X., Zou, L., Xia, J., Dou, M., Li, H., Song, Z., 2022. Untangling the effects of climate change and land use/cover change on spatiotemporal variation of evapotranspiration over China. J. Hydrol. 612, 128189. https://doi.org/10.1016/j.jhydrol.2022.128189.
Liang, X., Niu, Z., Li, X., 2023. Temporal and Spatial Variations of Extreme Climate Events in Northwestern China from 1960 to 2020. Sustainability 15, 14882. https://doi.org/10.3390/su152014882.
Lin, S., Huang, K., Sun, X., Song, C., Sun, J., Sun, S., Wang, G., Hu, Z., 2024. Estimates of net primary productivity and actual evapotranspiration over the Tibetan Plateau from the Community Land Model version 4.5 with four atmospheric forcing datasets. J. Plant Ecol. 17, rtae052. https://doi.org/10.1093/jpe/rtae052.
Liu, K., Wang, X., Wang, H., 2024. Quantifying the contributions of vegetation dynamics and climate factors to the enhancement of vegetation productivity in Northern China (2001–2020). Remote Sens 16, 3813. https://doi.org/10.3390/rs16203813.
Liu, R., Li, Y., Wang, Q., 2012. Variations in water and CO_2 fluxes over a saline desert in western China. Hydrol. Process 26, 513–522. https://doi.org/10.1002/hyp.8147.
Liu, S., Li, X., Xu, Z., Che, T., Xiao, Q., Ma, M., Liu, Q., Jin, R., Guo, J., Wang, L., Wang, W., Qi, Y., Li, H., Xu, T., Ran, Y., Hu, X., Shi, S., Zhu, Z., Tan, J., Zhang, Y., Ren, Z., 2018. The Heihe integrated Observatory network: a basin-scale land surface processes observatory in China. Vadose Zone J. 17, 1–21. https://doi.org/10.2136/vzj2018.04.0072.
Liu, S., Xu, Z., Che, T., Li, X., Xu, T., Ren, Z., Zhang, Y., Tan, J., Song, L., Zhou, J., Zhu, Z., Yang, X., Liu, R., Ma, Y., 2023. A dataset of energy, water vapor, and carbon exchange observations in oasis–desert areas from 2012 to 2021 in a typical endorheic basin. Earth Syst. Sci. Data 15, 4959–4981. https://doi.org/10.5194/essd-15-4959-2023.
Liu, W., Yang, L., Zhu, M., Adamowski, J.F., Barzegar, R., Wen, X., Yin, Z., 2021. Effect of elevation on variation in reference evapotranspiration under climate change in Northwest China. Sustainability 13, 10151. https://doi.org/10.3390/su131810151.
Luo, L., Ma, W., Zhuang, Y., Zhang, Y., Yi, S., Xu, J., Long, Y., Ma, D., Zhang, Z., 2018. The impacts of climate change and human activities on alpine vegetation and permafrost in the Qinghai-Tibet Engineering Corridor. Ecol. Indic. 93, 24–35. https://doi.org/10.1016/j.ecolind.2018.04.067.
Ma, N., Zhang, Y., 2022. Increasing Tibetan Plateau terrestrial evapotranspiration primarily driven by precipitation. Agric. For. Meteor. 317, 108887. https://doi.org/10.1016/j.agrformet.2022.108887.
Ma, Y.-J., Li, X.-Y., Liu, L., Yang, X.-F., Wu, X.-C., Wang, P., Lin, H., Zhang, G.-H., Miao, C.-Y., 2019. Evapotranspiration and its dominant controls along an elevation gradient in the Qinghai Lake watershed, northeast Qinghai-Tibet Plateau. J. Hydrol. 575, 257–268. https://doi.org/10.1016/j.jhydrol.2019.05.019.
Marrelec, G., Krainik, A., Duffau, H., Pélégrini-Issac, M., Lehéricy, S., Doyon, J., Benali, H., 2006. Partial correlation for functional brain interactivity investigation in functional MRI. NeuroImage 32, 228–237. https://doi.org/10.1016/j.neuroimage.2005.12.057.
Meng, X., Lyu, S., Li, Z., Ao, Y., Wen, L., Shang, L., Wang, S., Deng, M., Zhang, S., Zhao, L., Chen, H., Ma, D., Li, S., Shu, L., An, Y., Niu, H., 2023. Dataset of comparative observations for land surface processes over the semi-arid alpine grassland against Alpine lakes in the source region of the Yellow River. Adv. Atmos. Sci. 40, 1142–1157. https://doi.org/10.1007/s00376-022-2118-y.
Mu, Q., Zhao, M., Running, S.W., 2011. Improvements to a MODIS global terrestrial evapotranspiration algorithm. Remote Sens. Environ. 115, 1781–1800. https://doi.org/10.1016/j.rse.2011.02.019.
Niu, Z., He, H., Zhu, G., Ren, X., Zhang, L., Zhang, K., Yu, G., Ge, R., Li, P., Zeng, N., Zhu, X., 2019. An increasing trend in the ratio of transpiration to total terrestrial evapotranspiration in China from 1982 to 2015 caused by greening and warming. Agric. For. Meteor. 279, 107701. https://doi.org/10.1016/j.agrformet.2019.107701.
Niu, Z., He, H., Zhu, G., Ren, X., Zhang, L., Zhang, K., 2020. A spatial-temporal continuous dataset of the transpiration to evapotranspiration ratio in China from 1981 to 2015. Sci. Data 7, 369. https://doi.org/10.1038/s41597-020-00693-x.
Oki, T., Kanae, S., 2006. Global hydrological cycles and world water resources. Science 313, 1068–1072. https://doi.org/10.1126/science.1128845.
Piao, S., Wang, X., Park, T., Chen, C., Lian, X., He, Y., Bjerke, J.W., Chen, A., Ciais, P., Tømmervik, H., Nemani, R.R., Myneni, R.B., 2019. Characteristics, drivers and feedbacks of global greening. Nat. Rev. Earth Environ. 1, 14–27. https://doi.org/10.1038/s43017-019-0001-x.
Priestley, C.H.B., Taylor, R.J., 1972. On the assessment of surface heat flux and evaporation using large-scale parameters. Mon. Weather Rev. 100, 81–92. https://doi.org/10.1175/1520-0493(1972)100<0081:OTAOSH>2.3.CO;2.
Ren, M., Chen, W., Wang, H., 2022. Ecological policies dominated the ecological restoration over the core regions of Kubuqi desert in recent decades. Remote Sens 14, 5243. https://doi.org/10.3390/rs14205243.
Seneviratne, S.I., Corti, T., Davin, E.L., Hirschi, M., Jaeger, E.B., Lehner, I., Orlowsky, B., Teuling, A.J., 2010. Investigating soil moisture–climate interactions in a changing climate: A review.
Shao, R., Zhang, B., Su, T., Long, B., Cheng, L., Xue, Y., Yang, W., 2019. Estimating the increase in regional evaporative water consumption as a result of vegetation restoration over the Loess plateau, China. J. Geophys. Res. Atmospheres 124, 11783–11802. https://doi.org/10.1029/2019JD031295.
Shi, Y., Shen, Y., Kang, E., Li, D., Ding, Y., Zhang, G., Hu, R., 2007. Recent and future climate change in Northwest China. Clim. Change 80, 379–393. https://doi.org/10.1007/s10584-006-9121-7.
Wang, H., Li, X., Xiao, J., Ma, M., Tan, J., Wang, X., Geng, L., 2019b. Carbon fluxes across alpine, oasis, and desert ecosystems in northwestern China: the importance of water availability. Sci. Total Environ. 697, 133978. https://doi.org/10.1016/j.scitotenv.2019.133978.
Wang, H., Li, X., Ma, M., Geng, L., 2019a. Improving estimation of gross primary production in dryland ecosystems by a model-data fusion approach. Remote Sens 11, 225. https://doi.org/10.3390/rs11030225.
Wang, H., Li, X., Xiao, J., Ma, M., 2021. Evapotranspiration components and water use efficiency from desert to alpine ecosystems in drylands, 108283 Agric. For. Meteor. 298–299. https://doi.org/10.1016/j.agrformet.2020.108283.
Wang, L., Good, S.P., Caylor, K.K., 2014. Global synthesis of vegetation control on evapotranspiration partitioning. Geophys. Res. Lett. 41, 6753–6757. https://doi.org/10.1002/2014GL061439.
Wang, M., Yao, J., Chang, H., Liu, R., Xu, N., Liu, Z., Gong, H., Zheng, H., Wang, J., Guo, X., Cao, Y., Zhao, Y., Lu, H., 2025. Underground well water level observation grid dataset from 2005 to 2022. Sci. Data 12 (1), 728. https://doi.org/10.1038/s41597-025-04799-y.
Wang, N., Cheng, W., Wang, B., Liu, Q., Zhou, C., 2020. Geomorphological regionalization theory system and division methodology of China. J. Geogr. Sci. 30, 212–232. https://doi.org/10.1007/s11442-020-1724-9.
Wang, T., Zlotnik, V.A., 2012. A complementary relationship between actual and potential evapotranspiration and soil effects. J. Hydrol. 456–457, 146–150. https://doi.org/10.1016/j.jhydrol.2012.03.034.
Wang, W., Liao, Y., Wen, X., Guo, Q., 2013b. Dynamics of CO_2 fluxes and environmental responses in the rain-fed winter wheat ecosystem of the Loess Plateau, China. Sci. Total Environ. 461–462, 10–18. https://doi.org/10.1016/j.scitotenv.2013.04.068.
Wang, X., Ma, M., Li, X., Song, Y., Tan, J., Huang, G., Zhang, Z., Zhao, T., Feng, J., Ma, Z., Wei, W., Bai, Y., 2013a. Validation of MODIS-GPP product at 10 flux sites in northern China. Int. J. Remote Sens 34, 587–599. https://doi.org/10.1080/01431161.2012.715774.
Wang, T., Wu, Z., Wang, P., Wu, T., Zhang, Y., Yin, J., Yu, J., Wang, H., Guan, X., Xu, H., Yan, D., Yan, D., 2023. Plant-groundwater interactions in drylands: a review of current research and future perspectives. Agric. For. Meteor. 341, 109636. https://doi.org/10.1016/j.agrformet.2023.109636.
Webb, E.K., Pearman, G.I., Leuning, R., 1980. Correction of flux measurements for density effects due to heat and water vapour transfer. Q. J. R. Meteorol. Soc. 106, 85–100. https://doi.org/10.1002/qj.49710644707.
Yang, L., Feng, Q., Zhu, M., Wang, L., Alizadeh, M.R., Adamowski, J.F., Wen, X., Yin, Z., 2022. Variation in actual evapotranspiration and its ties to climate change and vegetation dynamics in northwest China. J. Hydrol. 607, 127533. https://doi.org/10.1016/j.jhydrol.2022.127533.
Yang, L., Feng, Q., Lu, T., Adamowski, J.F., Yin, Z., Hatami, S., Zhu, M., Wen, X., 2023. The response of agroecosystem water use efficiency to cropland change in northwest China's Hexi Corridor. Agric. Water Manag 276, 108062. https://doi.org/10.1016/j.agwat.2022.108062.
Yu, G., Ren, W., Chen, Z., Zhang, Leiming, Wang, Q., Wen, X., He, N., Zhang, Li, Fang, H., Zhu, X., Gao, Y., Sun, X., 2016. Construction and progress of Chinese terrestrial ecosystem carbon, nitrogen and water fluxes coordinated observation. J. Geogr. Sci. 26, 803–826. https://doi.org/10.1007/s11442-016-1300-5.
Yu, G.R., Wen, X.F., Sun, X.M., Tanner, B.D., Lee, X., Chen, J.Y., 2006. Overview of ChinaFLUX and evaluation of its eddy covariance measurement. Agric. For. Meteor. 137, 125–137. https://doi.org/10.1016/j.agrformet.2006.02.011.
Yu, L., Zhang, M., Wang, L., Qin, W., Jiang, D., Li, J., 2022. Variability of surface solar radiation under clear skies over Qinghai-Tibet Plateau: Role of aerosols and water vapor. Atmos. Environ. 287, 119286. https://doi.org/10.1016/j.atmosenv.2022.119286.
Zhang, D., Liu, X., Zhang, L., Zhang, Q., Gan, R., Li, X., 2020. Attribution of evapotranspiration changes in humid regions of China from 1982 to 2016. J. Geophys. Res. Atmospheres 125, e2020JD032404. https://doi.org/10.1029/2020JD032404.

Zhang, F., Li, H., Zhao, L., Zhang, L., Chen, Z., Zhu, J., Xu, S., Yang, Y., Zhao, X., Yu, G., Li, Y., 2021. An observation dataset of carbon, water and heat fluxes in an alpine wetland in Haibei (2004–2009). China Sci. Data 6, 50–59. https://doi.org/10.11922/csdata.2020.0033.zh.

Zhang, F., Li, H., Zhang, L., Li, J., Yang, Y., Yu, G., Li, Y., 2023a. A dataset of the observations of carbon, water and heat fluxes over an alpine shrubland in Haibei (2011–2020). China Sci. Data 8, 137–147 https://doi.org/DOI: 10.11922/11-6035.csd.2023.0013.zh.

Zhang, F., Si, M., Guo, X., Cao, G., Zhang, Z., 2023b. A dataset of the observations of carbon, water and heat fluxes over an alpine meadow in Haibei (2015–2020). China Sci. Data 8, 127–136. https://doi.org/10.11922/11-6035.csd.2023.0012.zh.

Zhang, K., Ma, J., Zhu, G., Ma, T., Han, T., Feng, L.L., 2017. Parameter sensitivity analysis and optimization for a satellite-based evapotranspiration model across multiple sites using Moderate Resolution Imaging Spectroradiometer and flux data. J. Geophys. Res. Atmospheres 122, 230–245. https://doi.org/10.1002/2016JD025768.

Zhang, Y., Kong, D., Gan, R., Chiew, F.H.S., McVicar, T.R., Zhang, Q., Yang, Y., 2019. Coupled estimation of 500 m and 8-day resolution global evapotranspiration and gross primary production in 2002–2017. Remote Sens. Environ. 222, 165–182.

Zhao, F., Wu, Y., Yao, Y., Sun, K., Zhang, X., Winowiecki, L., Vågen, T.-G., Xu, J., Qiu, L., Sun, P., Sun, Y., 2020. Predicting the climate change impacts on water-carbon coupling cycles for a loess hilly-gully watershed. J. Hydrol. 581, 124388. https://doi.org/10.1016/j.jhydrol.2019.124388.

Zhao, Y., Chen, Y., Wu, C., Li, G., Ma, M., Fan, L., Zheng, H., Song, L., Tang, X., 2023. Exploring the contribution of environmental factors to evapotranspiration dynamics in the Three-River-Source region, China. J. Hydrol. 626, 130222. https://doi.org/10.1016/j.jhydrol.2023.130222.

Zheng, H., Miao, C., Li, X., Kong, D., Gou, J., Wu, J., Zhang, S., 2022. Effects of vegetation changes and multiple environmental factors on evapotranspiration across China over the past 34 years. Earths Future 10, e2021EF002564. https://doi.org/10.1029/2021EF002564.

Zhu, G.F., Li, X., Su, Y.H., Zhang, K., Bai, Y., Ma, J.Z., Li, C.B., Hu, X.L., He, J.H., 2014. Simultaneously assimilating multivariate data sets into the two-source evapotranspiration model by Bayesian approach: application to spring maize in an arid region of northwestern China. Geosci. Model Dev. 7, 1467–1482. https://doi.org/10.5194/gmd-7-1467-2014.

Zhu, Y., Zheng, Z., Zhao, G., Zhu, J., Zhao, B., Sun, Y., Gao, J., Zhang, Y., 2025. Evapotranspiration increase is more sensitive to vegetation greening than to vegetation type conversion in arid and semi-arid regions of China. Glob. Planet. Change 244, 104634. https://doi.org/10.1016/j.gloplacha.2024.104634.

Zou, L., Zhan, C., Xia, J., Wang, T., Gippel, C.J., 2017. Implementation of evapotranspiration data assimilation with catchment scale distributed hydrological model via an ensemble Kalman Filter. J. Hydrol. 549, 685–702. https://doi.org/10.1016/j.jhydrol.2017.04.036.